Mesoscale Eddy Kinetic Energy Budgets and Transfers between Vertical Modes in the Agulhas Current

P. TEDESCO,[a] J. GULA,[a,b] P. PENVEN,[a] AND C. MÉNESGUEN[a]

[a] *Univ. Brest, CNRS, IRD, Ifremer, Laboratoire d'Océanographie Physique et Spatiale, IUEM, Brest, France*
[b] *Institut Universitaire de France, Paris, France*

ABSTRACT: Western boundary currents are hotspots of mesoscale variability and eddy–topography interactions, which channel energy toward smaller scales and eventually down to dissipation. Here, we assess the main mesoscale eddies energy sinks in the Agulhas Current region from a regional numerical simulation. We derive an eddy kinetic energy ($\overline{\text{EKE}}$) budget in the framework of the vertical modes. It accounts for energy transfers between energy reservoirs and vertical modes, including transfers channeled by topography. The variability is dominated by mesoscale eddies (barotropic and first baroclinic modes) in the path of intense mean currents. Eddy–topography interactions result in a major mesoscale eddy energy sink, along three different energy routes, with comparable importance: transfers toward bottom-intensified time-mean currents, generation of higher baroclinic modes, and bottom friction. The generation of higher baroclinic modes takes different forms in the Northern Agulhas Current, where it corresponds to nonlinear transfers to smaller vertical eddies on the slope, and in the Southern Agulhas Current, where it is dominated by a (linear) generation of internal gravity waves over topography. Away from the shelf, mesoscale eddies gain energy by an inverse vertical turbulent cascade. However, the Agulhas Current region remains a net source of mesoscale eddy energy due to the strong generation of eddies, modulated by the topography, especially in the Southern Agulhas Current. It shows that the local generation of mesoscale eddies dominates the net $\overline{\text{EKE}}$ budget, contrary to the paradigm of mesoscale eddies decay upon western boundaries.

KEYWORDS: Boundary currents; Eddies; Energy budget/balance; Internal waves; Kinetic energy; Mesoscale processes; Regional models

1. Introduction

Mesoscale eddies, with length scales on the order of the Rossby radius of deformation (Rd) or larger (Chelton et al. 2011), represent 90% of the kinetic energy (KE) reservoir. They are a major component of the global oceanic energy budget (Ferrari and Wunsch 2009). Understanding how the mesoscale eddies are sustained is a fundamental issue for the phenomenological and quantitative understanding of the global oceanic energy budget.

Wind drives the upper-ocean basin-scale mean circulation. Energy is then injected around the Rossby deformation radius Rd [$O(30–100)$ km] (Chelton et al. 1998), as mesoscale eddies, by instability processes of the mean currents. Oceanic dynamics at the mesoscale ($L \sim$ Rd) are characterized by the dominant effects of the rotation and stratification and are described by the quasigeostrophic balance (Charney 1971). In this dynamical regime, nonlinear interactions result in an inverse turbulent cascade (Rhines 1977, 1979), i.e., an energy transfer toward larger horizontal scales, and in an energy barotropization (Fu and Flierl 1980; Smith and Vallis 2001), i.e., an energy transfer from the first baroclinic (upper layers-intensified structure) to the barotropic (vertically homogeneous structures) vertical modes (Gill 1982).

An inverse turbulent cascade for the baroclinic energy has been inferred from the surface fields measured by satellite altimetry (Scott and Wang 2005; Scott and Arbic 2007). This inverse turbulent cascade occurring at the surface has been extensively investigated using satellite altimetry (Tulloch et al. 2011; Khatri et al. 2018) and models based on quasigeostrophic (Scott and Arbic 2007) and primitive equations (Schlösser and Eden 2007; Aluie et al. 2018).

Energy injected around Rd by the currents instabilities takes therefore the form of barotropic and baroclinic eddies. The barotropic component of this energy reservoir is partially dissipated by the bottom drag (Salmon 1980; Sen et al. 2008) and both barotropic and baroclinic components are partially dissipated by the wind stress (Eden and Dietze 2009; Seo et al. 2016; Renault et al. 2017). However, a large part of the energy reservoir dissipates at very small (micro) scales. The known energy paths from "balanced" motions (i.e., geostrophically balanced) at large scales toward "unbalanced" motions at smaller scales involve ageostrophic turbulence and interactions with internal gravity waves (Müller et al. 2005; Ferrari and Wunsch 2009).

Mesoscale eddies can lose energy to smaller scales by: scattering over rough bottom topography leading to internal lee waves generation (Nikurashin and Ferrari 2010, 2011), generation of internal lee waves along western boundaries (Clément et al. 2016), straining induced by the eddies–internal waves interactions (Rocha et al. 2018), hydraulic jumps related-dynamics generated by eddy–boundary waves interactions (Dewar and Hogg 2010; Gula and Zeitlin 2010), submesoscale horizontal shear instabilities triggered by topographic interactions (Dewar et al. 2015; Gula et al. 2016), and by the frontogenesis enhanced by the mesoscale eddy field background strain (Capet et al. 2008; Molemaker et al. 2010;

D'Asaro et al. 2011; Schubert et al. 2020) and possibly developing secondary frontal instabilities (Thomas et al. 2013). They can as well lose energy to the time-mean circulation by the so-called "Neptune effect" (Holloway 1987; Adcock and Marshall 2000).

Pointing toward the locations where mesoscale eddies predominantly lose energy provides a new perspective for investigating the mesoscale eddies energy loss. Zhai et al. (2010) suggested western boundaries as ubiquitous sinks of mesoscale eddy energy and pointed out that eddy–topography interactions could be responsible for the mesoscale eddy energy scattering toward smaller scales and eventually down to dissipation. Evans et al. (2020) provides a reference observational study case for the phenomenological understanding of the eddy–topography interactions involved in mesoscale eddies decay on western boundaries, in the absence of a western boundary current. However, the phenomenological and quantitative descriptions of these processes do not make yet a complete picture of the direct turbulent cascade, i.e., the energy transfer toward smaller scales (Ferrari and Wunsch 2010).

In this study, we evaluate the energetics of the mesoscale eddies by deriving an eddy kinetic energy (EKE) budget for the different vertical structures described by the traditional vertical modes (Gill 1982). This method allows us to characterize energy transfers between the different vertical modes and highlights the vertical component of the turbulent cascades, including the scattering, i.e., when energy is transferred to higher baroclinic modes.

Energy scattering has often been studied in the context of internal tides and lee waves generation (Kelly et al. 2010, 2012; Kelly 2016; Lahaye et al. 2020), but more seldomly in the context of mesoscale eddies. This framework approaches from a different angle the turbulent energy cascade to the one traditionally evaluated across horizontal scales by classic spectral analysis (Scott and Wang 2005; Schlösser and Eden 2007; Tulloch et al. 2011; Arbic et al. 2013, 2014; Khatri et al. 2018) and by coarse-graining methods (Aluie et al. 2018; Schubert et al. 2020).

Our mesoscale EKE budget is based on a regional numerical simulation of the Agulhas Current region, built upon a primitive equations model [Coastal and Regional Community (CROCO)] (Shchepetkin and McWilliams 2005; Debreu et al. 2012). The Agulhas Current is the most intense western boundary current of the Southern Hemisphere (Beal et al. 2015). It flows poleward along the South African coast, from the Mozambique Channel (26.5°S) to the southern African tip (37°S) where it separates from the continental shelf (Lutjeharms 2006), retroflects eastward and becomes the Agulhas Return Current when reentering in the south Indian Ocean (Lutjeharms and Ansorge 2001).

Based on its mesoscale variability, the Agulhas Current can be separated into Northern and Southern Agulhas Current (NAC and SAC) branches, connecting at Port Elizabeth (33.5°S) (Lutjeharms 2006; Paldor and Lutjeharms 2009). The mesoscale variability of the Northern Agulhas Current is low and mainly due to the intermittent passage of solitary meanders (Natal pulses) (Lutjeharms et al. 2003a) whereas mesoscale

eddies such as shear-edge eddies (Lutjeharms et al. 1989, 2003a) are common features of the Southern Agulhas Current. From the Agulhas Retroflection, large anticyclonic eddies (Agulhas rings) are generated and propagate into the southeast Atlantic Ocean (Lutjeharms 2006). A variety of mesoscale eddies are generated in the Agulhas Return Current permanent meanders (Gründlingh 1978; Lutjeharms and Valentine 1988). The Agulhas Current is therefore a suitable region for studying the mesoscale eddy dynamics, due to its intense local mesoscale variability and because it is suspected to channel the energy loss of remotely formed mesoscale eddies (Zhai et al. 2010).

In the present study, we aim to characterize the mesoscale eddy energetic dynamics in the Agulhas Current region, focusing on the NAC and the SAC. We address the following questions: 1) What is the vertical structure of eddy energy? 2) What is the mesoscale EKE budget? 3) What are the processes driving the mesoscale eddies generation, dissipation, and EKE transfer routes with higher baroclinic modes?

The study is organized as follows: the regional numerical simulation setup is presented and the mesoscale variability characteristics in the simulation are evaluated in section 2a. The vertical modes are defined and put into the context of eddy energy in section 2b. The derivation of the modal $\overline{\text{EKE}}$ budget is presented in section 2c. The vertical structure of the mesoscale eddy energy reservoirs is characterized in section 3, the mesoscale EKE budget is evaluated in section 4, and the main processes driving mesoscale eddies dynamics are characterized in section 5. The results are summarized and discussed in section 6.

2. Methods

a. The regional numerical simulations

We present in this section the regional numerical simulations and the modeled mesoscale eddy dynamics statistical evaluation against satellite and in situ data.

1) THE SIMULATION SETUP

The numerical model used in this study is the CROCO model. It is a free surface model, based on ROMS (Shchepetkin and McWilliams 2005), which solves the primitive equations in the Boussinesq and hydrostatic approximations using a terrain following coordinate system (Debreu et al. 2012).

We use a nesting approach with successive horizontal grid refinements from a parent grid resolution of $dx \sim 22.5$ km, covering most of the south Indian Ocean, to successive child grids resolutions of $dx \sim 7.5$ and 2.5 km (Fig. 1), using the online two-way nesting based on the AGRIF procedure (Debreu et al. 2012). The surface forcings are provided by a bulk formulation (Fairall et al. 1996) using the ERA-Interim reanalysis (Dee et al. 2011) with relative winds (Renault et al. 2017). The grids have 60 vertical levels stretched at the surface following Haidvogel and Beckmann's (1999) method.

The simulations are run for the 1993–2014 period after a spinup of 3 years ($dx \sim 22.5$ and 7.5 km) and 1 year ($dx \sim 2.5$ km) from their initial states. The three numerical
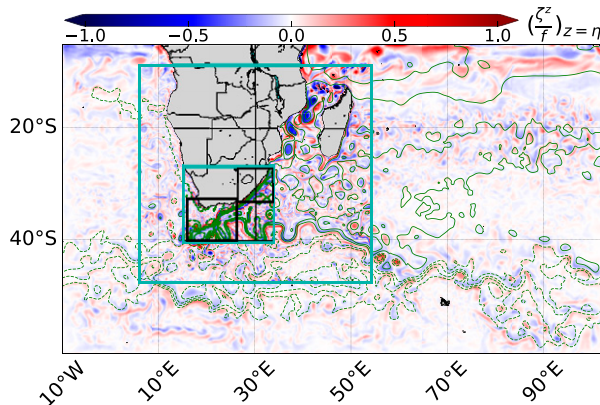
FIG. 1. Snapshot of the vertical component of the normalized surface relative vorticity ($|\zeta^z/f|_{z=\eta}$) in the Agulhas Current region as simulated by CROCO for the three nested domains (blue boxes): $dx \sim 22$, 7.5 and 2.5 km. The black boxes denote the regions of the NAC and SAC, on which this study focuses, which are further presented in section 2a(2). The green contours denote the −1-, −0.75-, −0.5-, −0.25-, 0.25-, 0.5-, 0.75-, and 1-m isolines of sea surface height. The relative vorticity and the sea surface height plotted inside each domain are computed from numerical outputs at the corresponding resolutions.

simulations and the numerical choices contributing to their realism (bathymetry, grid, parameterization of the turbulent closure, momentum and advective numerical schemes) are detailed in Tedesco et al. (2019).

In the present study, we investigate the mesoscale eddy energetics in the Agulhas Current region based on daily outputs during the 1994–99 period for the $dx \sim 2.5$-km grid.

2) OBSERVED AND MODELED MESOSCALE EDDIES

A generic measure of mesoscale turbulence is the eddy kinetic energy: $\overline{EKE} = (1/2)\overline{\|\mathbf{u}'\|^2}$, with $\mathbf{u}$ the horizontal velocity vector. The overbar denotes a time average and the prime denotes fluctuations relative to this average. Surface geostrophic $\overline{EKE}$ from the $dx \sim 2.5$-km grid is compared to the one derived from the altimetric data gridded onto a 1/4° regular grid by AVISO (Archiving, Validation, and Interpretation of Satellite Oceanographic Data) (Fig. 2, top). Both $\overline{EKE}$ are computed from geostrophic velocity derived from sea surface height anomalies.

A measure of the baroclinic component of the turbulence at depths is given by the eddy available potential energy: $\overline{EAPE} = (1/2)\overline{b'\zeta'}$, with b the buoyancy and ζ the vertical isopycnals displacement (Roullet et al. 2014). $\overline{EAPE}$ at 500-m depth from the $dx \sim 2.5$-km grid is compared to Roullet's (2020) atlas derived from ARGO data and gridded onto a 1/4° regular grid (Fig. 2, bottom).

Both $\overline{EKE}$ and the modeled $\overline{EAPE}$ are defined relative to a 1-yr running mean with a 1-month time step over the 1994–99 period and the observed $\overline{EAPE}$ is defined relative to a time average over the whole ARGO dataset ($\sim 10^6$ profiles over the last 15 years; Roullet 2020). The eddy component

defined by the 1-yr running mean filters the low-frequency dynamics and highlights the mesoscale dynamics, which corresponds to time scales from weeks to months.

Both modeled surface geostrophic $\overline{EKE}$ and 500-m depth $\overline{EAPE}$ have patterns and magnitudes in fairly good agreement with observations, denoting the known areas of low and high mesoscale variability in the Agulhas Current region (Fig. 2). The eddy energy is the highest along the Agulhas Current and the Agulhas Return Current [$\overline{EKE}$, $O(0.05$–$0.5)$ m^2 s^{-2} and $\overline{EAPE}$, $O(0.05$–$0.3)$ m^2 s^{-2}] and it is the lowest in the Southwest Indian Ocean Subgyre [$\overline{EKE}$, $O(0$–$0.05)$ m^2 s^{-2} and $\overline{EAPE}$, $O(0$–$0.05)$ m^2 s^{-2}] in the model and in the observations.

The Agulhas Current mesoscale variability has historically been characterized into northern (stable) and southern (unstable) branches connecting around Port Elizabeth (26°E) (Lutjeharms 2006; Paldor and Lutjeharms 2009). The stability of the Northern Agulhas branch (upstream of 26°E) is denoted by a lower eddy energy level [$\overline{EKE}$, $O(0$–$0.1)$ m^2 s^{-2} and $\overline{EAPE}$, $O(0$–$0.05)$ m^2 s^{-2}] than the southern branch, which has the highest eddy energy level of the Agulhas Current region [$\overline{EKE}$, $O(0.05$–$0.5)$ m^2 s^{-2} and $\overline{EAPE}$, $O(0.05$–$0.3)$ m^2 s^{-2}] in the model and in the observations. The eddy energy gradually increases downstream of the Southern Agulhas branch leading to a maximum at the Retroflection for the observed $\overline{EKE}$ model and both $\overline{EAPE}$s [$\overline{EKE}$, $O(0.2$–$0.5)$ m^2 s^{-2} and $\overline{EAPE}$, $O(0.2$–$0.3)$ m^2 s^{-2}]. The intense mesoscale variability of the Agulhas Return Current is denoted by a high eddy energy level, fairly uniform along the entire length of the Agulhas Return Current [$\overline{EKE}$, $O(0.1$–$0.15)$ m^2 s^{-2} and $\overline{EAPE}$, $O(0.05$–$0.15)$ m^2 s^{-2}], but lower than that of the Retroflection. The intense mesoscale variability along the Southern Agulhas Current, at the Agulhas Retroflection and along the Agulhas Return Current is visible at the surface ($\overline{EKE}$ in Fig. 2, top) and at 500-m depth ($\overline{EAPE}$ in Fig. 2, bottom), suggesting that mesoscale eddies have a vertical structure extending from the surface to at least 500-m depth in these areas.

A few discrepancies are noticeable between the modeled and observed surface $\overline{EKE}$s and 500-m depth $\overline{EAPE}$s. The modeled surface $\overline{EKE}$ has a higher magnitude along the entire Agulhas Current than the observed one (Fig. 2, top). It shows a moderate signal [$O(\sim 0.1)$ m^2 s^{-2}] along the northern branch, inshore of the 1000-m isobath, and a strong signal along the southern branch, that are both absent in the observations. However, the modeled $\overline{EKE}$ is highly similar to the observed one if we smooth the model sea surface height using a length scale of 100 km, which mimics the processing of altimetric data by AVISO (appendix A). It evidences the role played by horizontal scales < 100 km for the Southern Agulhas Current variability, which are not measured by AVISO.

The observed $\overline{EAPE}$ shows patterns of moderate amplitude [$O(\sim 0.05)$ m^2 s^{-2}] in the Subgyre that are absent from the model and a signal associated to the Agulhas Return Current [$O(0.05$–$0.1)$ m^2 s^{-2}] that covers a larger area than in the model (Fig. 2, bottom). These $\overline{EAPE}$ differences are not located specifically in undersampled areas (20–35 profiles)
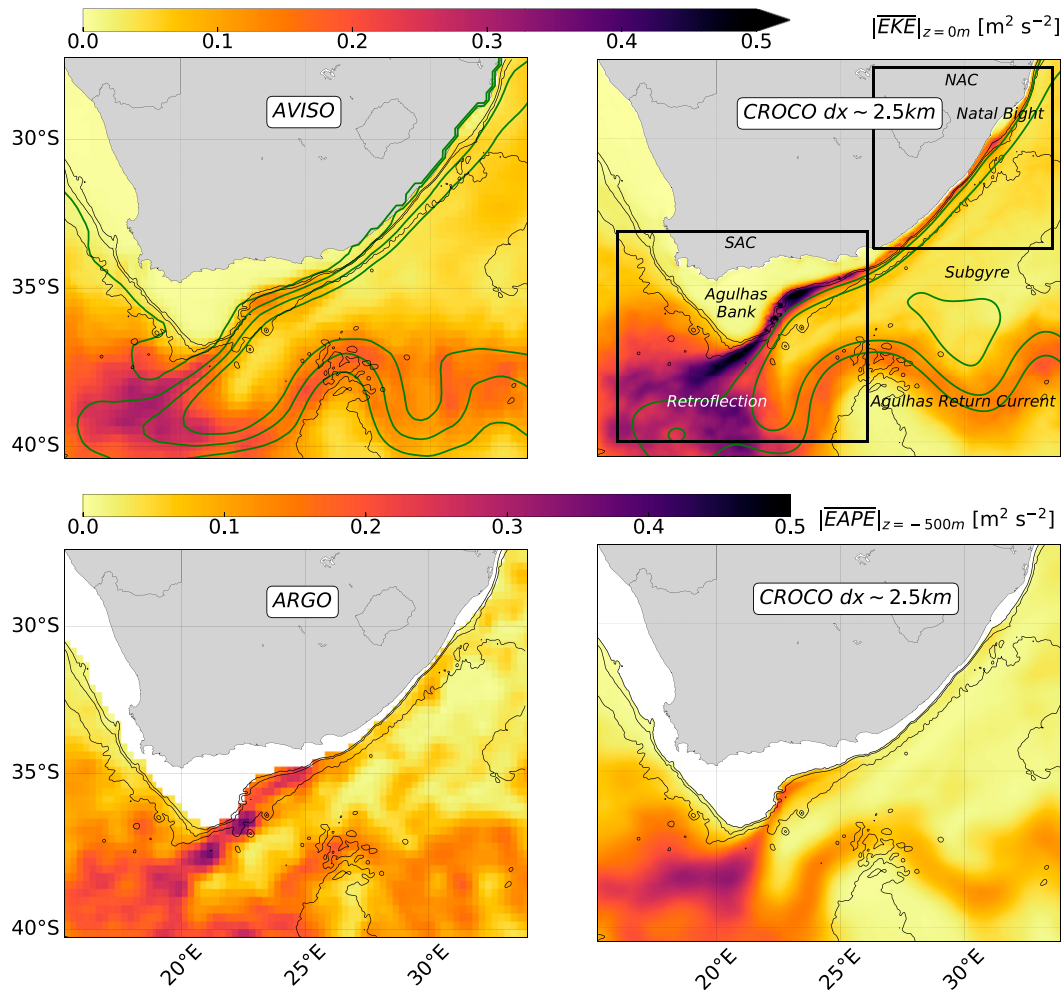
FIG. 2. (top) Surface $\overline{\mathrm{EKE}}$ (m^2 s^{-2}) for AVISO and for CROCO $dx \sim 2.5$ km and (bottom) 500-m depth $\overline{\mathrm{EAPE}}$ (m^2 s^{-2}) for ARGO (Roullet 2020) and for CROCO $dx \sim 2.5$ km. Both $\overline{\mathrm{EKE}}$ are defined from geostrophic velocities diagnosed from sea surface height fluctuations, where time fluctuations are defined relatively to a 1-yr running mean with a 1-month stepping over the 1994–99 period. The green contours denote the 0.25-, 0.5-, 0.75-, and 1-m isolines of mean sea surface height (top panels). For the modeled $\overline{\mathrm{EKE}}$ (top right panel), the black boxes delimit the NAC and SAC. Both $\overline{\mathrm{EAPE}}$ are defined following Roullet et al. (2014), for ARGO the time fluctuations are defined relative to the whole ARGO dataset (Roullet 2020) and for the model they are defined relatively to the 1-yr time running mean. The black contours denote the 500-, 1000-, and 3000-m isobaths (all panels). The modeled eddy energies denote the highest mesoscale variability along the Southern Agulhas Current (downstream of 26°E) and the Agulhas Return Current and the lowest one in the Southwest Indian Ocean Subgyre, consistently with the observations.

compared to the ARGO profiles density over the whole domain (10–60 profiles). The different definitions of the eddy components between the observed $\overline{\mathrm{EAPE}}$ (relative to a time average over the whole ARGO dataset collected over the last 15 years) and the modeled $\overline{\mathrm{EAPE}}$ (relative to a 1-yr running mean with a 1-month time step over a 5-yr period) could explain some of these differences. The modeled $\overline{\mathrm{EAPE}}$ defined relative to a 5-yr time average does not filter the inter-annual variability and show weaker differences with the observed $\overline{\mathrm{EAPE}}$ at these locations (not shown). However, the overall agreement in both $\overline{\mathrm{EAPE}}$ patterns and magnitudes, suggests that the fluctuation definition by a 1-yr running mean

is appropriate for investigating the mesoscale variability at depths in the Agulhas Current region.

Based on the different mesoscale eddy dynamics, we define two main areas in the Agulhas Current region: the NAC and SAC (Fig. 2, top right). The NAC covers the Northern Agulhas branch and the northern part of the Subgyre and is characterized by a low mesoscale variability. The SAC covers the Southern Agulhas branch, the Agulhas Retroflection, and the southern part of the Benguela Current and is characterized by a high mesoscale variability. In the following, the mesoscale eddy energetics are characterized separately in these two areas.

b. Vertical modes

We give in this section the mathematical definition of the vertical modes bases, and we derive the $\overline{\text{EKE}}$ and $\overline{\text{EAPE}}$ modal expansions and describe the vertical structures that they represent for the barotropic and the first nine baroclinic vertical modes.

1) DEFINITION OF THE VERTICAL MODES

We use the traditional vertical modes (Gill 1982). An alternative definition of vertical modes has been proposed by LaCasce (2017), using a condition of no bottom flow, but we prefer to use the traditional vertical modes to straightforwardly account for bottom-intensified flows (Stanley et al. 2020). In a continuously stratified ocean over a flat bottom, the vertical variability of the dynamical and state variables can be projected onto an orthogonal basis of n vertical modes [$\phi_n(z)$ or $\Phi_n(z)$] as follows:

$$\left[\mathbf{u}(\mathbf{x}, z, t), \frac{1}{\rho_0} p'(\mathbf{x}, z, t) \right] = \sum_{n=0}^{\infty} \left[\mathbf{u}_n(\mathbf{x}, t), \frac{1}{\rho_0} p'_n(\mathbf{x}, t) \right] \phi_n(z), \quad (1)$$

$$\left[w(\mathbf{x}, z, t), b'(\mathbf{x}, z, t) \right] = \sum_{n=0}^{\infty} \left[w_n(\mathbf{x}, t), b'_n(\mathbf{x}, t) \overline{N^2}(\mathbf{x}, z) \right] \Phi_n(z), \quad (2)$$

with p the total pressure, w the vertical velocity component, $\overline{N^2}$ the mean Brunt–Väisälä frequency, ($\mathbf{u}_n, p'_n, w_n, b'_n$) the respective modal amplitudes of the horizontal velocity components, the eddy pressure, the vertical velocity component and the eddy buoyancy for a vertical mode n.

Injecting the modal decomposition in the linearized quasigeostrophic equation leads to two equivalent Sturm–Liouville eigenvalue problems [Eqs. (3) and (6)]. The normal eigenfunctions solution are the $\phi_n(z)$ and $\Phi_n(z)$ vertical modes using linearized free-surface [$(w)_{z=\eta} = (\partial/\partial t)\eta$] and flat bottom [$(w)_{z=-H} = 0$] boundary conditions as in Kelly (2016):

$$\frac{\partial}{\partial z} \left[\frac{1}{\overline{N^2}} \frac{\partial}{\partial z} \phi_n \right] + \frac{1}{c_n^2} \phi_n = 0, \quad (3)$$

$$\left(\frac{\partial}{\partial z} \phi_n \right)_{z=\eta} = \left(\frac{-\overline{N^2}}{g} \phi_n \right)_{z=\eta}, \quad (4)$$

$$\left(\frac{\partial}{\partial z} \phi_n \right)_{z=-H} = 0, \quad (5)$$

$$\frac{\partial^2}{\partial z^2} \Phi_n + \frac{\overline{N^2}}{c_n^2} \Phi_n = 0, \quad (6)$$

$$(\Phi_n)_{z=\eta} = \left(\frac{c_n^2}{g} \frac{\partial}{\partial z} \Phi_n \right)_{z=\eta}, \quad (7)$$

$$(\Phi_n)_{z=-H} = 0, \quad (8)$$

with g the acceleration of gravity and c_n^2 the eigenvalues of the corresponding vertical modes.

The two modal bases are related via the continuity equation (9) and they respectively satisfy an orthogonality condition [Eqs. (10) and (11)]:

$$\phi_n = \frac{\partial}{\partial z} \Phi_n, \quad (9)$$

$$\int_{-H}^{\eta} \phi_m \phi_n \, dz = \delta_{mn} h, \quad (10)$$

$$\frac{g}{c_n^2} (\Phi_m \Phi_n)_{z=\eta} + \int_{-H}^{\eta} \frac{\overline{N^2}}{c_n^2} \Phi_m \Phi_n \, dz = \delta_{mn} h, \quad (11)$$

with δ_{mn} the usual Kronecker symbol and $h = \eta + H$ the water column depth.

The modal amplitudes of the variables are derived by combining their modal expansions [Eqs. (1) and (2)] with the mode's orthogonality conditions [Eqs. (10) and (11)]:

$$\left[\mathbf{u}_n(\mathbf{x}, t), \frac{1}{\rho_0} p'_n(\mathbf{x}, t) \right] = \frac{1}{h} \int_{-H}^{\eta} \left[\mathbf{u}(\mathbf{x}, z, t), \frac{1}{\rho_0} p'(\mathbf{x}, z, t) \right] \phi_n(z) \, dz, \quad (12)$$

$$w_n(\mathbf{x}, t) = \frac{1}{h c_n^2} \left[\int_{-H}^{\eta} \overline{N^2} w(\mathbf{x}, z, t) \Phi_n(z) \, dz + g(w \Phi_n)_{z=\eta} \right], \quad (13)$$

$$b'_n(\mathbf{x}, t) = \frac{1}{h c_n^2} \left[\int_{-H}^{\eta} b'(\mathbf{x}, z, t) \Phi_n(z) \, dz + g\left(\frac{b'}{\overline{N^2}} \Phi_n \right)_{z=\eta} \right]. \quad (14)$$

The vertical modes are related to horizontal scales via their eigenvalues, which are good approximations of the Rossby baroclinic deformation radii (Chelton et al. 1998):

$$\text{Rd}_{n \geq 1} = \frac{c_n}{|f|} \approx \frac{1}{n \pi |f|} \int_{-H}^{\eta} N(\mathbf{x}, z) \, dz, \quad (15)$$

with f the Coriolis parameter.

The traditional vertical modes definition is based on a flat bottom assumption, which is relaxed in regional numerical simulations. This leads to spatially varying Brunt–Väisälä frequency and therefore vertical modes [$\overline{N^2}(\mathbf{x}, z)$, $\phi_n(\mathbf{x}, z)$ and $\Phi_n(\mathbf{x}, z)$] and thus to non-null vertical modes horizontal gradients. These gradients represent an intermodal coupling forced by the stratification–topographic spatial variations, which is of particular interest for internal tides generation and scattering (Kelly et al. 2010, 2012; Kelly 2016; Lahaye et al. 2020). The validity of the traditional vertical modes definition is confirmed in the context of the $dx \sim 2.5$-km regional simulation for the 1994–99 period in appendix B. The barotropic and the first 9 baroclinic modes capture 80%–100% of the variability of the modeled dynamics. The adequate resolution of the 10 first vertical modes by the $dx \sim 2.5$-km grid has also been confirmed (not shown), validating its choice for investigating the mesoscale eddy dynamics.

2) MODAL EXPANSIONS OF EDDY ENERGIES ($\overline{\mathrm{EKE}_n}$ AND $\overline{\mathrm{EAPE}_n}$)

In the following, we derive the $\overline{\mathrm{EKE}}$ and $\overline{\mathrm{EAPE}}$ modal expansions (subsequently referred as $\overline{\mathrm{EKE}_n}$ and $\overline{\mathrm{EAPE}_n}$) and we describe and classify the vertical structures corresponding to the barotropic and 9 first baroclinic vertical modes of the two modal bases (ϕ_n and Φ_n).

The $\overline{\mathrm{EKE}_n}$ and $\overline{\mathrm{EAPE}_n}$, expressed with the free-surface boundary condition, respectively depend on the two vertical mode bases (ϕ_n and Φ_n) as follows:

$$\overline{\int_{-H}^{\eta} \mathrm{EKE}\, dz} = \overline{\int_{-H}^{\eta} \frac{1}{2} \left\| \sum_{n=0}^{\infty} (\mathbf{u}_n' \phi_n) \sum_{m=0}^{\infty} (\mathbf{u}_m' \phi_m) \right\|^2 dz}$$

$$= \sum_{n=0}^{\infty} \frac{\overline{h}}{2} \overline{\|\mathbf{u}_n'\|^2} = \sum_{n=0}^{\infty} \overline{\mathrm{EKE}_n}, \qquad (16)$$

$$\overline{\int_{-H}^{\eta} \mathrm{EAPE}\, dz} = \overline{\int_{-H}^{\eta} \frac{1}{2} \sum_{n=0}^{\infty} \left(b_n' \overline{N^2} \Phi_n\right) \sum_{m=0}^{\infty} (\zeta_m' \Phi_m)\, dz}$$

$$= \sum_{n=0}^{\infty} \left[\frac{1}{2} \overline{b_n' \zeta_n'} h c_n^2 - \underbrace{\sum_{m=0}^{\infty} \frac{g}{2} \overline{b_n' \zeta_m'} (\Phi_n \Phi_m)_{z=\eta}}_{\overline{C_{nm}}:\ \text{intermodal coupling at the free surface}} \right]$$

$$= \sum_{n=0}^{\infty} \left(\overline{\mathrm{EAPE}_n} + \overline{C_{nm}} \right). \qquad (17)$$

The $\overline{\mathrm{EAPE}_n}$ expression (17) is more complex than $\overline{\mathrm{EKE}_n}$ (16), because it involves a term of intermodal coupling at the free surface ($\overline{C_{nm}}$). It originates from the orthogonality condition of the Φ_n bases expressed with the free-surface boundary condition (11).

The two vertical modes bases (ϕ_n and Φ_n), and therefore $\overline{\mathrm{EKE}_n}$ and $\overline{\mathrm{EAPE}_n}$, correspond to different vertical structures for a given vertical mode n (Fig. 3). The $\overline{\mathrm{EKE}}$ (Fig. 3, top) decomposes into a barotropic mode (ϕ_0) representing a vertically homogeneous structure, a first baroclinic mode (ϕ_1) representing a structure intensified in the upper layers, above the main thermocline (1000 m for a 5000-m-deep ocean), and into higher baroclinic modes (ϕ_{2-4}) representing structures intensified over surface layers [$O(100)$ m] whose vertical extension becomes shallower with the baroclinicity level (we extend the description of the 2–4 baroclinic modes to the ninth baroclinic mode, even though they are not all plotted in Fig. 3 for reasons of readability of the figure). The $\overline{\mathrm{EAPE}}$ (Fig. 3, bottom), decomposes into a barotropic mode (Φ_0) representing a structure linearly decreasing from a maximum at the free-surface toward zero at the bottom, a first baroclinic mode (Φ_1) representing a structure intensified at intermediate depths of $O(500–2000)$ m, and into higher baroclinic modes (Φ_{2-9}) representing structures intensified below the surface.

Based on these three categories, both ϕ_0 and Φ_1 correspond to vertical structures energized at depth and the ϕ_{1-9} and Φ_{2-9} correspond to surface-intensified vertical structures. Φ_0 represents a category of its own, of surface-intensified vertical structures whose energy linearly decreases with depth. This last category originates from the use of the free-surface

boundary condition (7), but its physical meaning remains unclear especially since it accounts for almost no potential energy (Ferrari and Wunsch 2009).

c. The mean modal eddy kinetic energy ($\overline{\mathrm{EKE}_n}$) budget

We develop in this section the $\overline{\mathrm{EKE}_n}$ evolution equation corresponding to the classic $\overline{\mathrm{EKE}}$ evolution equation, but derived in the vertical modes frame. We also present the physical processes related to the different contributions to the $\overline{\mathrm{EKE}_n}$ budget.

1) DERIVATION OF THE $\overline{\mathrm{EKE}_n}$ EQUATION

The modal kinetic energy equation is decomposed into a mean and an eddy part, in the same way than the classical $\overline{\mathrm{EKE}}$ equation (Harrison and Robinson 1978; Gula et al. 2016), such as: $\overline{\mathrm{KE}_n} = \mathrm{MKE}_n + \overline{\mathrm{EKE}_n}$, with $\overline{\mathrm{KE}_n} = \overline{\int_{-H}^{\eta} (1/2) \|\mathbf{u}_n\|^2\, dz}$ the mean modal KE, $\mathrm{MKE}_n = \int_{-H}^{\overline{\eta}} (1/2) \|\overline{\mathbf{u}}_n\|^2\, dz$ the modal KE of the mean flow, and $\overline{\mathrm{EKE}_n} = \overline{\int_{-H}^{\eta} (1/2) \|\mathbf{u}_n'\|^2\, dz}$ the mean modal EKE.

The CROCO model solves the primitive equations under the Boussinesq and hydrostatic approximations:

$$\frac{\partial}{\partial t} \mathbf{u} + \mathbf{u} \cdot \nabla_H \mathbf{u} + w \frac{\partial}{\partial z} \mathbf{u} + f \mathbf{k} \wedge \mathbf{u} = -\frac{1}{\rho_0} \nabla_H p + \mathbf{V} + \mathbf{D}, \qquad (18)$$

$$\frac{\partial}{\partial z} p + g \rho = 0, \qquad (19)$$

$$\nabla_H \cdot \mathbf{u} + \frac{\partial}{\partial z} w = 0, \qquad (20)$$

with $\rho(\mathbf{x}, z, t)$ the density variation relative to the density reference, $\rho_0 = 1025$ kg m^{-3}; $\mathbf{V}$ the vertical mixing expressed as $\mathbf{V} = \partial/\partial z[K_{Mv}(\partial \mathbf{u}/\partial z)]$ with K_{Mv} the diffusivity; and $\mathbf{D}$ the horizontal dissipation.

The momentum equations are first projected into a vertical mode n following Kelly (2016). Equations (18) and (20) are multiplied by ϕ_n and vertically integrated. Equation (19) is multiplied by Φ_n and vertically integrated, leading to

$$h \left(\frac{\partial}{\partial t} \mathbf{u} \right)_n + \int_{-H}^{\eta} \left(\mathbf{u} \cdot \nabla_H \mathbf{u} + w \frac{\partial}{\partial z} \mathbf{u} \right) \phi_n\, dz + f \mathbf{k} \wedge h \mathbf{u}_n$$

$$= -\frac{1}{\rho_0} \int_{-H}^{\eta} (\nabla_H p) \phi_n\, dz + h \mathbf{V}_n + h \mathbf{D}_n, \qquad (21)$$

$$h p_n' + h c_n^2 b_n' - g \left(\frac{b'}{N^2} \Phi_n \right)_{z=\eta} = 0, \qquad (22)$$

$$\nabla_H \cdot (h \mathbf{u}_n) - \sum_{m=0}^{\infty} \mathbf{u}_m \cdot \int_{-H}^{\eta} \phi_m \nabla_H \phi_n\, dz + h w_n$$

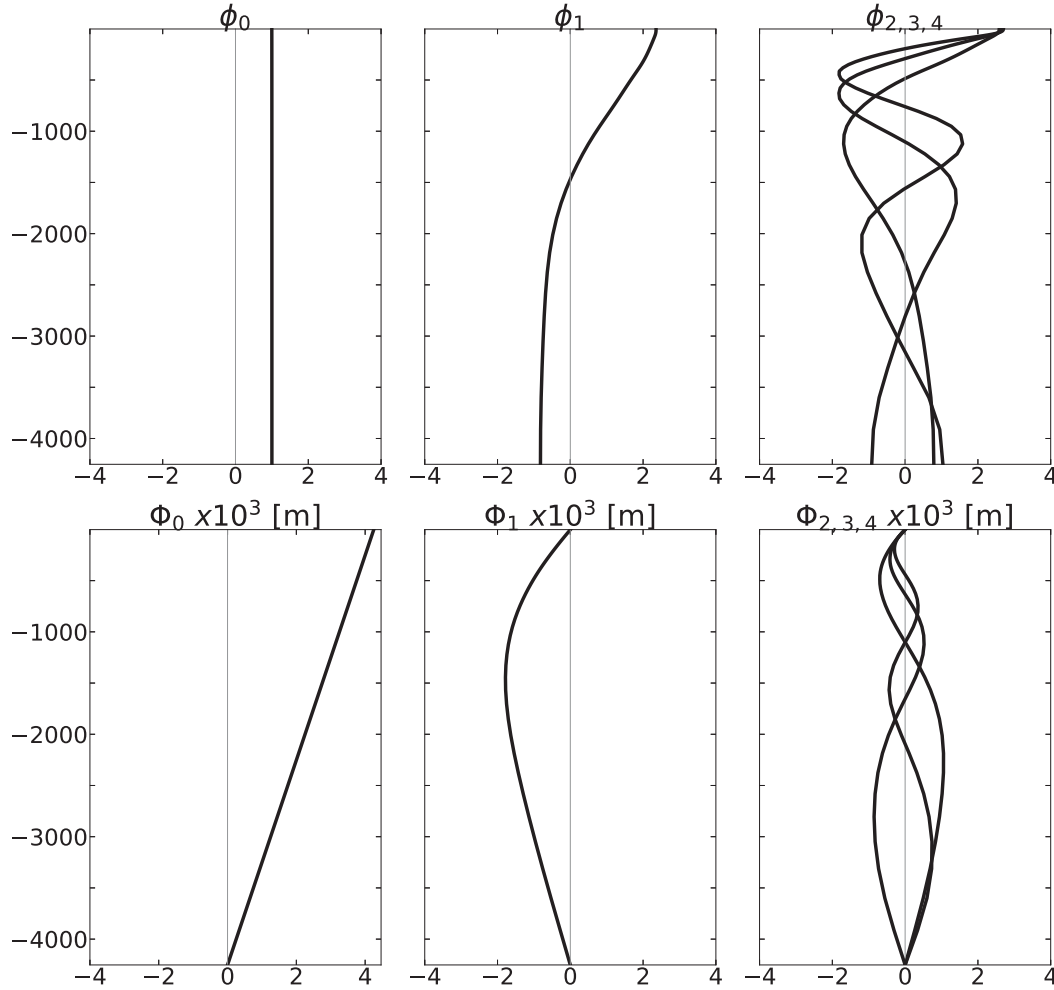$$- \nabla_H \eta \cdot (\mathbf{u} \phi_n)_{z=\eta} = 0. \qquad (23)$$

FIG. 3. Profiles of $\overline{\text{EKE}}$ [$\phi_n(\mathbf{x}, z)$] and $\overline{\text{EAPE}}$ [$\Phi_n(\mathbf{x}, z)$ (m)] barotropic modes ($n = 0$), first baroclinic modes ($n = 1$) and higher baroclinic modes ($n = 2, 3, 4$) at a given location of the $dx \sim 2.5$-km grid. Vertical modes are derived from the local modeled Brunt–Väisälä frequency [$\overline{N^2}(\mathbf{x}, z)$ (s^{-2})] averaged using a 1-yr running mean with a 1-month stepping over the 1994–99 period. The (ϕ_0, Φ_1) categories represent structures energized at depth, the (ϕ_{1-4}, Φ_{2-4}) categories represent surface-intensified vertical structures and the Φ_0 represents surface-intensified linearly decreasing vertical structures.

The $\overline{\text{EKE}}_n$ equation is obtained by doing $\overline{\text{EKE}}_n = \overline{\text{KE}}_n -$ MKE$_n$ in the same way as for the classic $\overline{\text{EKE}}$ equation (Gula et al. 2016). The $\overline{\text{KE}}_n$ equation is derived by taking the inner product between the modal horizontal velocity vector ($\mathbf{u}_n$) and the modal horizontal momentum equation (21), and by

time averaging. The MKE$_n$ equation is derived by taking the inner product between the mean modal horizontal velocity vector ($\overline{\mathbf{u}}_n$) and the mean modal horizontal momentum equations [(21) time averaged]. The $\overline{\text{EKE}}_n$ equation is finally obtained by subtracting MKE$_n$ to $\overline{\text{KE}}_n$, such as

$$\underbrace{\overline{\mathbf{u}'_n \cdot h\left(\frac{\partial}{\partial t}\,\mathbf{u}\right)_n}}_{\text{Time rate}} + \underbrace{\overline{\mathbf{u}'_n \cdot \int_{-H}^{\eta}\left(\mathbf{u}\cdot\nabla_H\mathbf{u} + w\,\frac{\partial}{\partial z}\,\mathbf{u}\right)\phi_n\,dz}}_{\text{Advection}} - \underbrace{\overline{\mathbf{u}}_n\cdot\left(f\mathbf{k}\wedge\overline{h\mathbf{u}_n}\right)}_{\text{Coriolis}} = -\underbrace{\overline{\mathbf{u}'_n\cdot\frac{1}{\rho_0}\int_{-H}^{\eta}(\nabla_H p)\phi_n\,dz}}_{\text{Pressure gradient}} + \underbrace{\overline{\mathbf{u}'_n\cdot(h\mathbf{V}_n)}}_{\text{Vertical mixing}} + \underbrace{\overline{\mathbf{u}'_n\cdot(h\mathbf{D}_n)}}_{\text{Numerical dissipation}}\;.$$

$$(24)$$

The advection and the pressure gradient terms of the $\overline{\text{EKE}}_n$ equation (24) can be further decomposed into different contributions. The first-order accuracy of the analytical

development of the contributions of the horizontal and vertical advection terms (25) and (26) and of the pressure gradient term (27) is shown in appendix C.

Using the modal expansion of the horizontal velocities (1), the horizontal advection term is decomposed into six contributions: the horizontal Reynolds stress within a vertical mode n ($\overline{\mathrm{HRS}_n}$), the horizontal advection of $\overline{\mathrm{EKE}_n}$, the complementary term to the advection of $\overline{\mathrm{EKE}_n}$, the horizontal triad interactions and the advective eddy–eddy and eddy–mean interactions on slopes, as follows:

$$
\overline{\mathbf{u}'_n \cdot \int_{-H}^{\eta} (\mathbf{u} \cdot \nabla_H \mathbf{u})\phi_n \, dz} = \underbrace{\overline{\mathbf{u}'_n \cdot (\mathbf{u}'_n \cdot \nabla_H)\overline{\mathbf{u}}_n} \int_{-H}^{\overline{\eta}} \phi_n \phi_n \phi_n \, dz}_{\overline{\mathrm{HRS}_n}} + \underbrace{\nabla_H \cdot \left[\overline{(\overline{\mathbf{u}}_n + \mathbf{u}'_n)\frac{1}{2}\|\mathbf{u}'_n\|^2} \int_{-H}^{\overline{\eta}} \phi_n \phi_n \phi_n \, dz \right]}_{\text{Horizontal advection of } \overline{\mathrm{EKE}_n}}
$$

$$
- \underbrace{\frac{1}{2}\overline{\|\mathbf{u}'_n\|^2 \nabla_H \cdot \left(\mathbf{u}_n \int_{-H}^{\overline{\eta}} \phi_n \phi_n \phi_n \, dz \right)}}_{\text{Complement to the horizontal advection of } \overline{\mathrm{EKE}_n}}
$$

$$
+ \underbrace{\sum_{m \neq n}^{\infty} \sum_{l \neq n}^{\infty} \left[\underbrace{\overline{\mathbf{u}'_n \cdot (\mathbf{u}'_m \cdot \nabla_H)\mathbf{u}'_l}}_{\text{Eddy–eddy interactions}} + \underbrace{\overline{\mathbf{u}'_n \cdot (\overline{\mathbf{u}}_m \cdot \nabla_H)\mathbf{u}'_l} + \overline{\mathbf{u}'_n \cdot (\mathbf{u}'_m \cdot \nabla_H)\overline{\mathbf{u}}_l}}_{\text{Eddy–mean interactions}} \right] \int_{-H}^{\overline{\eta}} \phi_n \phi_m \phi_l \, dz}_{\text{Horizontal triad interactions}}
$$

$$
+ \underbrace{\sum_{m=0}^{\infty} \sum_{l=0}^{\infty} \overline{\mathbf{u}'_n \cdot \mathbf{u}'_l \mathbf{u}'_m} \cdot \int_{-H}^{\overline{\eta}} \phi_n \phi_m \nabla_H \phi_l \, dz}_{\text{Advective eddy–eddy interactions on slopes}} + \underbrace{\sum_{m=0}^{\infty} \sum_{l=0}^{\infty} \overline{\mathbf{u}'_n \cdot (\mathbf{u}'_l \overline{\mathbf{u}}_m + \overline{\mathbf{u}}_l \mathbf{u}'_m)} \cdot \int_{-H}^{\overline{\eta}} \phi_n \phi_m \nabla_H \phi_l \, dz}_{\text{Advective eddy–mean interactions on slopes}}. \tag{25}
$$

Using the modal expansion of the horizontal and vertical velocities (1) and (2), the relation between the two vertical mode basis (9) and the Sturm–Liouville equation (6), the vertical advection term is decomposed into three contributions: the vertical Reynolds stress within a vertical mode n ($\overline{\mathrm{VRS}_n}$), the vertical advection of $\overline{\mathrm{EKE}_n}$, and the vertical triad interactions, as follows:

$$
\overline{\mathbf{u}'_n \cdot \int_{-H}^{\eta} \left(w \frac{\partial}{\partial z} \mathbf{u} \right)\phi_n \, dz} = -\underbrace{\overline{\mathbf{u}'_n \cdot (\overline{\mathbf{u}}_n w'_n)} \int_{-H}^{\overline{\eta}} \frac{N^2}{c_n^2} \phi_n \Phi_n \Phi_n \, dz}_{\overline{\mathrm{VRS}_n}} - \underbrace{\overline{w_n \|\mathbf{u}'_n\|^2} \int_{-H}^{\overline{\eta}} \frac{N^2}{c_n^2} \phi_n \Phi_n \Phi_n \, dz}_{\text{Vertical advection of } \overline{\mathrm{EKE}_n}}
$$

$$
- \underbrace{\sum_{m \neq n} \sum_{l \neq n} \overline{\mathbf{u}'_n \cdot (\mathbf{u}_l w_m)} \int_{-H}^{\overline{\eta}} \frac{N^2}{c_n^2} \cdot \phi_n \Phi_m \Phi_l \, dz}_{\text{Vertical triad interactions}}. \tag{26}
$$

Using Leibniz's rule, the modal expansion of the pressure anomaly (1), the orthogonality condition of the vertical modes (10), the modal continuity equation (23) and the modal hydrostatic equation (22), the pressure gradient term is decomposed into 4 contributions: the eddy-pressure work, the vertical buoyancy fluxes within a vertical mode n ($\overline{\mathrm{VBF}_n}$), the eddy–eddy interactions on slopes and a small term reflecting the free-surface contribution, as follows:

$$
-\overline{\mathbf{u}'_n \cdot \frac{1}{\rho_0} \int_{-H}^{\eta} (\nabla_H p)\phi_n \, dz} = -\underbrace{\nabla_H \cdot \frac{1}{\rho_0} \left(\overline{h \mathbf{u}'_n p'_n} \right)}_{\text{Eddy–pressure work}} + \underbrace{\overline{c_n^2 h b'_n w'_n} - \overline{g w'_n \left(\frac{b'}{N^2} \Phi_n \right)}_{z=\eta}}_{\overline{\mathrm{VBF}_n}}
$$

$$
+ \underbrace{\sum_{m=0}^{\infty} \frac{1}{\rho_0} \left(\overline{\mathbf{u}'_m p'_n} \right) \cdot \int_{-H}^{\overline{\eta}} \phi_m \nabla_H \phi_n \, dz - \sum_{m=0}^{\infty} \frac{1}{\rho_0} \left(\overline{\mathbf{u}'_n p'_m} \right) \cdot \int_{-H}^{\overline{\eta}} \phi_n \nabla_H \phi_m \, dz}_{\text{Pressure gradient eddy–eddy interactions on slopes}}
$$

$$
- \frac{1}{\rho_0} \underbrace{\overline{p'_n \nabla_H \eta \cdot (\mathbf{u}'\phi_n)_{z=\eta}}}_{\text{Contribution of the free surface} \ll 1}. \tag{27}
$$

The final expression of the $\overline{\text{EKE}_n}$ equation is obtained by replacing the different contributions originating from the horizontal and vertical advection terms (25) and (26) and from the pressure gradient term (27) into the former expression of the $\overline{\text{EKE}_n}$ equation (24). The terms of the final expression of the $\overline{\text{EKE}_n}$ equation are organized into the four following categories:

$$
\underbrace{A}_{\substack{\overline{\text{EKE}_n}\text{ evolution}}} = \underbrace{B}_{\substack{\text{Transfers between}\\\text{the }\overline{\text{EKE}_n},\ \text{MKE}_n\text{ and }\overline{\text{EPE}_n}\\\text{reservoirs}}} + \underbrace{C}_{\substack{\text{Transfers between}\\\text{vertical modes}}} + \underbrace{D}_{\substack{\overline{\text{EKE}_n}\text{ generation}\\\text{and dissipation}}}
\tag{28}
$$

leading to the final expression of the $\overline{\text{EKE}_n}$ equation:

$$
\underbrace{\overline{\mathbf{u}'_n \cdot \left[h\left(\frac{\partial}{\partial t}\,\mathbf{u}\right)_n \right]}}_{\text{Time rate (A.1)}}
$$

$$
+ \underbrace{\underbrace{\nabla_H \cdot \frac{1}{\rho_0}\left(\overline{h\mathbf{u}'_n p'_n}\right)}_{\text{Eddy–pressure work (A.2)}} + \underbrace{\nabla_H \cdot \left[\overline{(\overline{\mathbf{u}}_n + \mathbf{u}'_n)\frac{1}{2}\|\mathbf{u}'_n\|^2} \int_{-H}^{\overline{\eta}} \phi_n\phi_n\phi_n\,dz \right] - \overline{(\overline{w}_n + w'_n)\|\mathbf{u}'_n\|^2} \int_{-H}^{\overline{\eta}} \frac{N^2}{c_n^2}\phi_n\Phi_n\Phi_n\,dz}_{\text{Advection of }\overline{\text{EKE}_n}\text{ (A.3)}}}_{\overline{\text{EKE}_n}-\text{fluxes divergence (A.2+A.3)}}
$$

$$
= \underbrace{-\overline{\mathbf{u}'_n\cdot(\mathbf{u}'_n\cdot\nabla_H)\overline{\mathbf{u}}_n}\int_{-H}^{\overline{\eta}}\phi_n\phi_n\phi_n\,dz}_{\text{MKE}_n\to\overline{\text{EKE}_n}\ (\overline{\text{HRS}_n})\ \text{(B.1)}} + \underbrace{\overline{\mathbf{u}'_n\cdot(\overline{\mathbf{u}}_n w'_n)}\int_{-H}^{\overline{\eta}}\frac{N^2}{c_n^2}\phi_n\Phi_n\Phi_n\,dz}_{\text{MKE}_n\to\overline{\text{EKE}_n}\ (\overline{\text{VRS}_n})\ \text{(B.2)}} + \underbrace{\overline{c_n^2 h b'_n w'_n} - \overline{g w'_n\left(\frac{b'}{N^2}\Phi_n\right)}_{z=\eta}}_{\overline{\text{EPE}_n}\to\overline{\text{EKE}_n}\ (\overline{\text{VBF}_n})\ \text{(B.3)}}
$$

$$
\underbrace{-\sum_{m\ne n}^{\infty}\sum_{l\ne n}^{\infty}\underbrace{\overline{\mathbf{u}'_n\cdot(\mathbf{u}'_m\cdot\nabla_H)\mathbf{u}'_l}}_{\text{Eddy–eddy interactions (C.1.1a)}} + \underbrace{\overline{\mathbf{u}'_n\cdot(\overline{\mathbf{u}}_m\cdot\nabla_H)\mathbf{u}'_l} + \overline{\mathbf{u}'_n\cdot(\mathbf{u}'_m\cdot\nabla_H)\overline{\mathbf{u}}_l}}_{\text{Eddy–mean interactions (C.1.1b)}}\int_{-H}^{\overline{\eta}}\phi_n\phi_m\phi_l\,dz}_{\text{Horizontal triad interactions (C.1.1)}}
$$

$$
+ \underbrace{\sum_{m\ne n}^{\infty}\sum_{l\ne n}^{\infty}\overline{\mathbf{u}'_n\cdot(\mathbf{u}_l w_m)}\int_{-H}^{\overline{\eta}}\frac{N^2}{c_n^2}\phi_n\Phi_m\Phi_l\,dz}_{\text{Vertical triad interactions (C.1.2)}} - \underbrace{\sum_{m=0}^{\infty}\sum_{l=0}^{\infty}\overline{\mathbf{u}'_n\cdot\mathbf{u}'_l\mathbf{u}'_m}\cdot\int_{-H}^{\overline{\eta}}\phi_n\phi_m\nabla_H\phi_l\,dz}_{\text{Advective eddy–eddy interactions on slopes (C.2)}}
$$

$$
- \underbrace{\sum_{m=0}^{\infty}\sum_{l=0}^{\infty}\overline{\mathbf{u}'_n\cdot(\mathbf{u}'_l\overline{\mathbf{u}}_m + \overline{\mathbf{u}}_l\mathbf{u}'_m)}\cdot\int_{-H}^{\overline{\eta}}\phi_n\phi_m\nabla_H\phi_l\,dz}_{\text{Advective eddy–mean interactions on slopes (C.3)}}
$$

$$
+ \underbrace{\sum_{m=0}^{\infty}\frac{1}{\rho_0}\left(\overline{\mathbf{u}'_m p'_n}\right)\cdot\int_{-H}^{\overline{\eta}}\phi_m\nabla_H\phi_n\,dz - \sum_{m=0}^{\infty}\frac{1}{\rho_0}\left(\overline{\mathbf{u}'_n p'_m}\right)\cdot\int_{-H}^{\overline{\eta}}\phi_n\nabla_H\phi_m\,dz}_{\text{Pressure gradient eddy–eddy interactions on slopes (C.4)}}
$$

$$
-\frac{1}{\rho_0}\underbrace{\overline{p'_n\nabla_H\eta\cdot(\mathbf{u}'\phi_n)}_{z=\eta}}_{\text{Contribution of the free surface}\ll1\ \text{(C.5)}} + \underbrace{\frac{1}{2}\|\mathbf{u}'_n\|^2\nabla_H\cdot\left(\mathbf{u}_n\int_{-H}^{\overline{\eta}}\phi_n\phi_n\phi_n\,dz\right)}_{\text{Complement to the horizontal advection of }\overline{\text{EKE}_n}\ \text{(C.6)}}
$$

$$
+ \underbrace{\overline{\mathbf{u}'_n\cdot(h\mathbf{V}_n)}}_{\text{Vertical mixing (D.1)}} + \underbrace{\overline{\mathbf{u}'_n\cdot(h\mathbf{D}_n)}}_{\text{Numerical dissipation (D.2)}} + \underbrace{\overline{\mathbf{u}}_n\cdot\left(f\mathbf{k}\wedge\overline{h\mathbf{u}_n}\right)}_{\text{Coriolis (D.3)}}.
\tag{29}
$$

The method used to compute the $\overline{EKE_n}$ budget using the $dx \sim 2.5$-km grid numerical outputs and the numerical accuracy of the $\overline{EKE_n}$ budget closure are presented in appendix D.

2) THE DIFFERENT CONTRIBUTIONS TO THE $\overline{EKE_n}$ EQUATION (TERMS A, B, C, AND D)

In the following, we interpret in terms of physical processes the different contributions of the $\overline{EKE_n}$ budget [Eq. (29)].

Terms A, $\overline{EKE_n}$ evolution:

- Time rate (A.1): Evolution of the $\overline{EKE}$ storage within the vertical mode n over time, which tends toward zero for a long time average. It does not have a significant contribution to our mesoscale $\overline{EKE_n}$ ($\overline{EKE_{0-1}}$: defined as the sum of the barotropic and first baroclinic modes) budget (appendix D).
- $\overline{EKE_n}$ fluxes divergence (A.2 + A.3): $\overline{EKE_n}$ transport, which can be interpreted as the $\overline{EKE_n}$ fluxes at the domain boundaries when integrated over a closed volume. It has two contributions: the eddy-pressure work, which represents the energy transport done by the linear components of the dynamics, and the advection of $\overline{EKE_n}$ by the total 3D flow, which represents the energy transport done by the advection (nonlinear component of the dynamics). In the frame of linear theories of internal waves (Kelly et al. 2010, 2012; Kelly 2016), Rossby waves (Masuda 1978) and of open-ocean dynamics (Zhai et al. 2010) the eddy–pressure work is kept as the only contribution to the $\overline{EKE_n}$ transport.

Terms B, transfers between the $\overline{EKE_n}$, MKE$_n$, and $\overline{EPE_n}$ reservoirs:

- MKE$_n \rightarrow \overline{EKE_n}$ ($\overline{HRS_n}$) term (B.1): Horizontal Reynolds stress–mean flow nonlinear interactions within a vertical mode n. It is the counterpart of the horizontal Reynolds stress ($\overline{HRS}$), which is used as an indicator of horizontal shear instabilities such as the barotropic (Gula et al. 2015a,b) and the centrifugal/inertial (Gula et al. 2016) instabilities.
- MKE$_n \rightarrow \overline{EKE_n}$ ($\overline{VRS_n}$) term (B.2): Vertical Reynolds stress–mean flow nonlinear interactions within a vertical mode n. It is the counterpart of the vertical Reynolds stress ($\overline{VRS}$), which is used as an indicator of vertical-shear-related instabilities such as Kelvin–Helmholtz or symmetric instability (Thomas et al. 2013).
- $\overline{EPE_n} \rightarrow \overline{EKE_n}$ ($\overline{VBF_n}$) term (B.3): Vertical buoyancy fluxes reflecting eddy energy conversion between the potential and kinetic reservoirs within a vertical mode n. It is the counterpart of the $\overline{VBF}$ term, which is used as an indicator of the baroclinic instability at meso (horizontal scales of Rd or larger) and submesoscale [horizontal scales of $O(0.1\text{–}10)$ km] (McWilliams 2016).

Terms C, transfers between vertical modes:

- Horizontal triad interactions (C.1.1): Eddy–eddy (C.1.1a) and eddy–mean (C.1.1b) nonlinear interactions between vertical modes. The intermodal coupling is represented by

the triad coefficient: $\int_{-H}^{\overline{\eta}} \phi_n \phi_m \phi_l \, dz$ and corresponds to the following vertical modes combinations: $(n = m \neq l)$, $(n = l \neq m)$, $(n \neq m = l)$, and $(n \neq m \neq l)$. These triad interactions are the counterpart of the horizontal component of the advective operator that transfers KE across scales (Salmon 1980; Vallis 2006). The eddy–eddy interactions represent the turbulent energy cascades and the eddy–mean interactions represent unforced energy transfers across scales and reservoirs.

- Vertical triad interactions (C.1.2): Eddy–total flow nonlinear interactions between vertical modes. The intermodal coupling is represented by the triad coefficient: $\int_{-H}^{\overline{\eta}} \left(N^2/c_n^2 \right) \phi_n \Phi_m \Phi_l \, dz$ and corresponds to the following vertical modes combinations: $(n = m \neq l)$, $(n = l \neq m)$, $(n \neq m = l)$ and $(n \neq m \neq l)$. These triad interactions point toward the contribution of the vertical advection to the turbulent energy cascades and to the unforced energy transfers across scales and reservoirs, as a complement to the horizontal triad interactions (C.1.1).

- Advective eddy–eddy flow interactions on slopes (C.2): Eddy–eddy nonlinear interactions between vertical modes associated with stratification–topography horizontal gradients. The intermodal coupling is represented by $\int_{-H}^{\overline{\eta}} \phi_n \phi_m \nabla_H \phi_l \, dz$ and corresponds to the vertical modes combinations: $(n = m \neq l)$, $(n = l \neq m)$, $(n \neq m = l)$, and $(n \neq m \neq l)$. This term points toward eddy–eddy and eddy–waves nonlinear interactions forced by the stratification–topography horizontal gradient. The $(n = m = l)$ case does not represent an energy transfer between reservoirs or vertical structures and likely corresponds to $\overline{EKE_n}$ advection, but it does not represent a main contribution to our $\overline{EKE_{0-1}}$ budget (Fig. 8).

- Advective eddy–mean interactions on slopes (C.3): Eddy–mean nonlinear interactions between vertical modes associated with stratification–topography horizontal gradients. The intermodal coupling is represented by $\int_{-H}^{\overline{\eta}} \phi_n \phi_m \nabla_H \phi_l \, dz$ and corresponds to the vertical modes combinations: $(n = m \neq l)$, $(n = l \neq m)$, $(n \neq m = l)$, and $(n \neq m \neq l)$. These interactions are mainly interpreted as eddies driving mean currents over sloping topography (Holloway 1987; Adcock and Marshall 2000) if the vertical modes combination $(n = m = l)$ has an equal contribution as the other ones to the energy transfer. Indeed, bottom-intensified flows decompose into a barotropic mode, allowing a nonzero bottom velocity, and into baroclinic modes, to cancel or to shape velocity in the upper layers, as tested by Stanley et al. (2020).

- Pressure gradient eddy–eddy interactions on slopes (C.4): Eddy–eddy linear interactions between vertical modes associated with stratification–topography horizontal gradients. The intermodal coupling is represented by $\int_{-H}^{\overline{\eta}} \phi_m \nabla_H \phi_n \, dz$ and $\int_{-H}^{\overline{\eta}} \phi_n \nabla_H \phi_m \, dz$ and corresponds to the vertical modes combination: $(n \neq m)$. This term points toward eddy–eddy and eddy–waves linear interactions forced by the stratification–topography horizontal gradients. These interactions correspond

to eddies inducing topographic Rossby waves on a sloping bottom and to eddies scattering over seamounts, topographic features, accidents, and slopes leading to the generation of internal gravity waves—such as lee waves (Gill 1982; Nikurashin and Ferrari 2010). This latter process is similar to the tidal scattering leading to internal tides generation (Kelly et al. 2010, 2012; Kelly 2016).

- Contribution of the free-surface $\ll 1$ (C.5): Eddy–eddy interactions between vertical modes at the free surface. This term has a mathematical origin [Eq. (23)], but it has a negligible effect on our $\overline{\mathrm{EKE}}_{0-1}$ budget (appendix D).

- Complement to the advection of $\overline{\mathrm{EKE}}_n$ (C.6): Term derived from the horizontal advection contribution, which allows to write the horizontal advection of $\overline{\mathrm{EKE}}_n$ as a divergence of $\overline{\mathrm{EKE}}_n$ flux [Eq. (25)]. This contribution does not cancel out in the framework of the vertical modes, contrary to the $\overline{\mathrm{EKE}}$ budget where the continuity equation is used to cancel out a similar contribution (Harrison and Robinson 1978). However, it has a small effect on our $\overline{\mathrm{EKE}}_{0-1}$ budget (appendix D).

Terms D, $\overline{\mathrm{EKE}}_n$ generation and dissipation:

- Vertical mixing (D.1): $\overline{\mathrm{EKE}}_n$ dissipation and/or generation by wind stress, interior vertical mixing, and bottom drag. The wind stress dissipates surface energy regardless of the oceanic structures (Hughes and Wilson 2008; Renault et al. 2018) and the bottom drag dissipates barotropic (Fu and Flierl 1980; Sen et al. 2008) and non-null baroclinic $\overline{\mathrm{EKE}}$.

- Numerical dissipation (D.2): $\overline{\mathrm{EKE}}_n$ dissipation by the horizontal implicit viscosity of the model. This numerical contribution has a negligible effect on our $\overline{\mathrm{EKE}}_{0-1}$ budget (appendix D).

- Coriolis term (D.3): $\overline{\mathrm{EKE}}_n$ dissipation and/or generation by the Coriolis term. This contribution does not cancel out in the framework of the vertical modes, contrary to the $\overline{\mathrm{EKE}}$ budget (Harrison and Robinson 1978). However, this numerical contribution has a negligible effect on our $\overline{\mathrm{EKE}}_{0-1}$ budget (appendix D).

3. Results I: Characterization of the vertical structure of eddy energy reservoirs ($\overline{\mathrm{EKE}}$ and $\overline{\mathrm{EAPE}}$)

We characterize in this section the vertical structure of the eddy energy reservoirs ($\overline{\mathrm{EKE}}$ and $\overline{\mathrm{EAPE}}$) using the vertical modes in the Agulhas Current region, with a particular focus on the NAC and SAC regions.

a. Mesoscale eddy energy reservoirs

The vertical structure of the mesoscale eddy energy reservoirs is characterized from the different $\overline{\mathrm{EKE}}$ and $\overline{\mathrm{EAPE}}$ partitionings between the vertical modes categories ($n = 0$, $n = 1$, and $n = 2$–9) (Fig. 4).

The $\overline{\mathrm{EKE}}$ mainly partitions into the ϕ_0 and ϕ_1 categories [$O(70–100)\%$] and weakly into the ϕ_{2-9} category [$<O(30)\%$]. $\overline{\mathrm{EKE}}$ is uniformly equipartitioned between the ϕ_0 and ϕ_1 categories over the Agulhas Current region, except in the path

of the Agulhas Current and in the Agulhas Retroflection where the ϕ_0 category dominates. $\overline{\mathrm{EAPE}}$ has a more variable vertical partitioning than $\overline{\mathrm{EKE}}$. It partitions significantly into the three vertical modes categories [Φ_0: (0–60)%, Φ_1: (15–89)%, and Φ_{2-9}: (5–57)%]. $\overline{\mathrm{EAPE}}$ mostly partitions into the Φ_1 category [$O(70–89)\%$] in areas of intense mean circulation (Agulhas Current, Agulhas Retroflection, Agulhas Return Current and the southern part of the Benguela Current) and it significantly partitions into the Φ_0 and Φ_{2-9} categories [$O(40–60)\%$] in the Subgyre.

The $\overline{\mathrm{EKE}}$ vertical partitioning is consistent with the mesoscale eddies vertical structure being dominated by the barotropic (ϕ_0) and first baroclinic (ϕ_1) modes (Wunsch 1997; Smith and Vallis 2001) and with mesoscale eddies being the most energetic eddy flows (Ferrari and Wunsch 2009). The $\overline{\mathrm{EAPE}}$ partitions predominantly into Φ_1 category in areas dominated by mesoscale eddies (Fig. 4). The $\overline{\mathrm{EAPE}}$ vertical partitioning into the Φ_0 and Φ_{2-9} categories in the Subgyre, denotes a variability at small vertical scales confined to the surface, which is not visible from the $\overline{\mathrm{EKE}}$ partitioning.

b. Local vertical structures of eddy energy in the NAC and SAC regions

The NAC and SAC regions are divided in subareas of documented variability: the Alongshore Northern Agulhas Current (A) and the Northern Subgyre (B) (both in the NAC) and the Eastern Agulhas Bank Bight (C), the Agulhas Retroflection (D), and the Benguela area (E) (all in the SAC). In these subareas, the $\overline{\mathrm{EKE}}$ and $\overline{\mathrm{EAPE}}$ vertical partitionings correspond to one of the three following combinations: $\phi_0 > \phi_1$ and $\Phi_1 > (\Phi_0, \Phi_{2-9})$ (in A, C, and D), $\phi_0 \sim \phi_1$ and $\Phi_0 \sim \Phi_1 \sim \Phi_{2-9}$ (in B), and $\phi_0 \sim \phi_1$ and $\Phi_1 > (\Phi_0, \Phi_{2-9})$ (in E).

1) THE NORTHERN AGULHAS CURRENT (NAC)

In the NAC, eddies have different vertical structures between areas in the path of the Agulhas Current (A) and offshore—away from the topographic constraint and from the Agulhas Current—in the Subgyre (B) (Fig. 4).

The A area shows an $\overline{\mathrm{EKE}}$ and an $\overline{\mathrm{EAPE}}$ mostly in one vertical mode: ϕ_0 [$O(60)\%$] $> \phi_1$ [$O(30)\%$] and Φ_1 [$O(60)\%$] $> (\Phi_0, \Phi_{2-9})$ [$O(40)\%$]. Both vertical partitionings denote that variability is dominated by mesoscale eddies having a $\overline{\mathrm{EKE}}$ barotropic component larger than the first baroclinic one.

The mesoscale variability of the Northern branch of the Agulhas Current is mainly due to the punctual passage of Natal pulses along the Northern branch of the Agulhas Current (Lutjeharms 2006). They are solitary cyclonic eddies, of diameters of about 50–200 km, extending over the whole water column, which are generated at the Natal Bight (~31°E) (Lutjeharms et al. 2003a; Elipot and Beal 2015).

The B area shows an $\overline{\mathrm{EKE}}$ equipartitioned between the ϕ_0 [$O(46)\%$] and ϕ_1 [$O(42)\%$] categories and an $\overline{\mathrm{EAPE}}$ equipartitioned between the Φ_0 [$O(30)\%$], Φ_1 [$O(40)\%$] and Φ_{2-9} [$O(30)\%$] categories. The $\overline{\mathrm{EKE}}$ partitioning ($\phi_0 \sim \phi_1$)
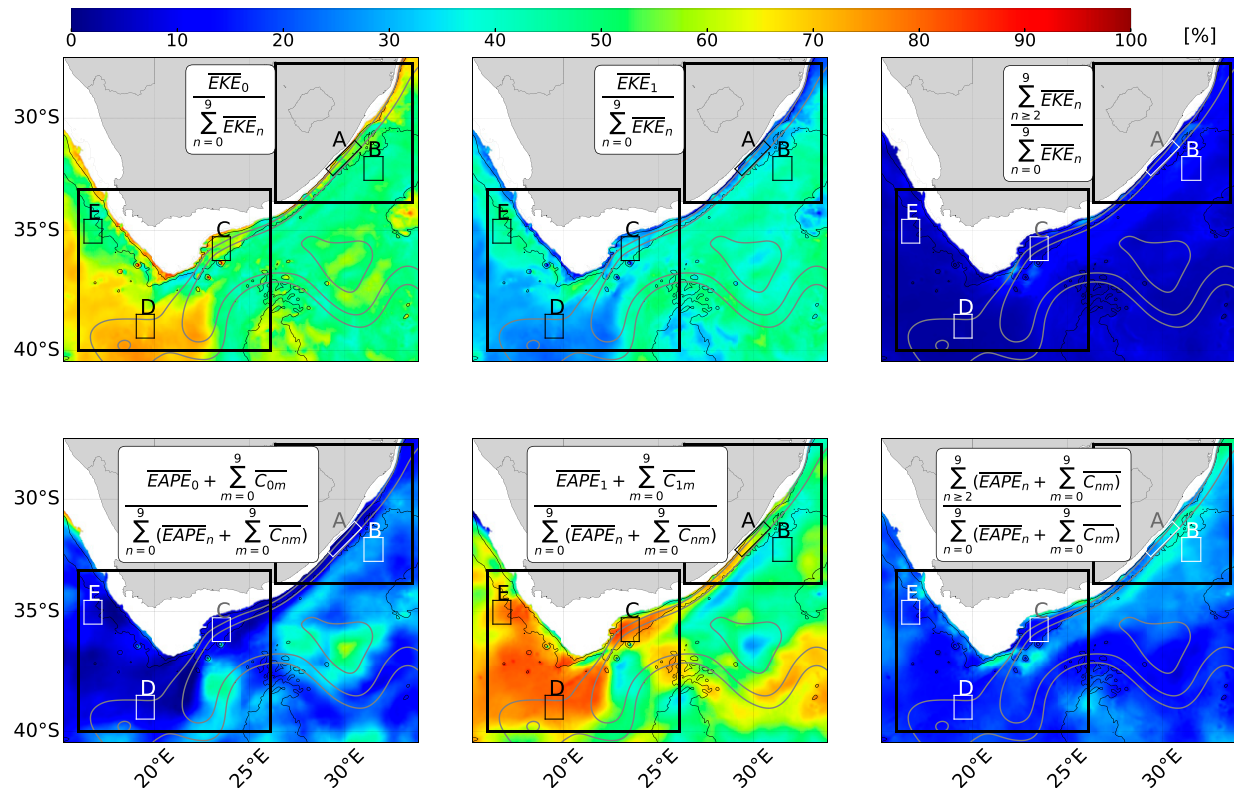
FIG. 4. (top) $\overline{EKE}$ and (bottom) $\overline{EAPE}$ partitioning (%) between the vertical mode categories ($n = 0$, 1, and 2–9). The gray contours denote the 0.25-, 0.5-, and 0.75-m isolines of mean sea surface height and the black contours denote the 1000- and 3000-m isobaths. The five ($1° \times 1°$) boxes denote the areas A–E discussed in section 3b. The mesoscale eddies reservoir is represented by the barotropic (ϕ_0) and first baroclinic $\overline{EKE}$ modes (ϕ_1) and the first baroclinic $\overline{EAPE}$ mode (Φ_1).

corresponds to surface-intensified profiles with a lower energy level at depths than in the A, C, and D areas ($\phi_0 > \phi_1$), because the relative proportions of ϕ_0 and ϕ_1 drive the rate of decrease of energy with depth. The $\overline{EAPE}$ partitioning corresponds to profiles intensified at the surface (Φ_{2-9}) and at intermediate depths (Φ_1). $\overline{EKE}$ and $\overline{EAPE}$ vertical partitionings denote mesoscale eddies, having similar $\overline{EKE}$ barotropic and first baroclinic components, and eddies of higher baroclinic modes confined at the surface, denoted by $\overline{EAPE}$ high baroclinic modes.

The Subgyre (B) mesoscale variability corresponds, in part, to the propagation of mesoscale eddies generated in the Agulhas Return Current or in the Subtropical South Indian Gyre, because of the absence of local generation mechanism. The small vertical scales confined to the surface can denote mixed-layer-related variability, which significance has recently been highlighted in the Subgyre region (Schubert et al. 2020).

2) THE SOUTHERN AGULHAS CURRENT

In the SAC, eddies have more homogeneous vertical structures between areas in the path of the Agulhas Current (C and D) and away, in the southern part of the Benguela Current (E) (Fig. 4).

The C and D areas show an $\overline{EKE}$ and $\overline{EAPE}$ mostly in one vertical mode: ϕ_0 [$O(55–70)$%] > ϕ_1 [$O(27–37]$%] and Φ_1 [$O(75–80)$%] $\gg$ Φ_0, Φ_{2-9} [$O(20–25)$%]. Both vertical partitionings denote that variability is dominated by mesoscale eddies having an $\overline{EKE}$ barotropic component larger than the first baroclinic one, similarly to A area. It can be hinted from the surface geostrophic $\overline{EKE}$ and the 500-m depth $\overline{EAPE}$ (Fig. 2).

The Eastern Agulhas Bank Bight (C) high mesoscale variability is due to several types of documented features (Lutjeharms et al. 1989, 2003a). One type includes the shear-edge eddy (Lutjeharms et al. 1989; Goschen and Schumann 1990), which is a quasi-permanent cyclonic eddy, of diameters of about 50–100 km, extending at least over the first 500 m depth (Lutjeharms et al. 2003a). This area is also affected by the trapping of Natal pulses (Rouault and Penven 2011; Krug et al. 2014). The Agulhas Retroflection (D) is known for its extremely high mesoscale variability due to the Agulhas rings, which are anticyclones of diameters of $O(200)$ km (Duncombe Rae 1991), which have a strong barotropic component (Van Aken et al. 2003).

The E area shows an $\overline{EKE}$ equipartitioned between the ϕ_0 [$O(50)$%] and ϕ_1 [$O(45)$%] categories and an $\overline{EAPE}$ mostly into one category Φ_1 [$O(75)$%] > Φ_0, Φ_{2-9} [$O(25)$%]. Both

vertical partitionings denote that variability is dominated by mesoscale eddies having a lower $\overline{EKE}$ barotropic component compared to the C and D areas (as hinted from Fig. 2).

The Benguela area (E) mesoscale variability results from locally and remotely generated mesoscale eddies (Lutjeharms 2006). The area is affected by the Agulhas rings drifting northeastward and by cyclonic mesoscale eddies developing along the coastal upwelling fronts at topographically controlled locations (~33°S) (Lutjeharms 2006). Typical features are cyclonic mesoscale eddies of diameters about 60 km in areas deeper than 2500-m depth and about 20 km in area between 500 and 2500 m (Rubio et al. 2009).

The eddy vertical structure allows us to presume about the leading-order processes of the mesoscale eddy dynamics. Mesoscale eddies ($\phi_0 > \phi_1$ and Φ_1 or $\phi_0 \sim \phi_1$ and Φ_1) are likely generated by barotropic or mixed barotropic–baroclinic instability processes of the Agulhas Current (A, C, and D areas) and of the Benguela Current (E area). Locally generated mesoscale eddies likely interact with the mean current as well as with topography where the Agulhas Current is strongly constrained by the shelf (A and C areas). They also likely interact with eddies of higher baroclinic modes, where Φ_{2-9} is significant (B area). The low variability associated with higher baroclinic modes in A and C areas does not necessarily indicates that mesoscale eddies weakly interact with higher baroclinic modes. It could suggest that energy of higher baroclinic modes is locally dissipated and transported away or it could come from the vertical partitioning of eddy energies not emphasizing the larger energy level of the high baroclinic modes in C area than in B area (Fig. 4), because C area is located where the total eddy energies are the most intense of the Agulhas Current region (Fig. 2). We further investigate the eddy dynamics at the origins of the different eddy vertical structures in the following section using our $\overline{EKE}_n$ budget.

4. Results II: Mesoscale eddy kinetic energy ($\overline{EKE_{0-1}}$) budgets in the NAC and SAC regions

We characterize in this section the mesoscale eddy dynamics using the mesoscale $\overline{EKE}_n$ ($\overline{EKE_{0-1}}$) budget [Eq. (29) and section 3a]. The $\overline{EKE_{0-1}}$ budget is defined as the sum of the barotropic ($\overline{EKE_0}$) and first baroclinic ($\overline{EKE_1}$) budgets. We limit our characterization of the $\overline{EKE}$ budget to the complete mesoscale reservoir, i.e., barotropic and first baroclinic modes together, because we aim to evaluate the mesoscale eddy energy sinks. The study of energy transfers and equilibration within the mesoscale reservoir, i.e., between the barotropic and first baroclinic modes, would need a separate study and it is not addressed here.

We first evaluate the net $\overline{EKE_{0-1}}$ budget, on the left-hand side of the $\overline{EKE_{0-1}}$ equation [A terms in Eq. (29)], and then the different $\overline{EKE_{0-1}}$ sources and sinks, on the right-hand side of the $\overline{EKE_{0-1}}$ equation [B, C, and D terms in Eq. (29)]. We first define subareas in the NAC and SAC regions with different mesoscale eddy dynamics using the net $\overline{EKE_{0-1}}$ budget (A terms). We then characterize, in term of physical processes, the mesoscale eddy dynamics in these subareas

using the main $\overline{EKE_{0-1}}$ sources and sinks (B, C, and D terms).

a. Net $\overline{EKE_{0-1}}$ budgets (terms A.2 and A.3)

The left-hand side of the $\overline{EKE_{0-1}}$ equation (29) mainly accounts for the divergence of the $\overline{EKE_{0-1}}$ fluxes (A.2 and A.3 terms) (cf. appendix D). The divergence of the $\overline{EKE_{0-1}}$ fluxes equals the sum of the local $\overline{EKE_{0-1}}$ sources and sinks (B, C, and D terms) and therefore represents the net $\overline{EKE_{0-1}}$ budget. It indicates a net local $\overline{EKE_{0-1}}$ source (>0) or a net local $\overline{EKE_{0-1}}$ sink (<0) according to its sign. It can also be interpreted as the budget of incoming and outgoing fluxes due to: the eddy-pressure work (A.2) and the advection of $\overline{EKE_{0-1}}$ by the total flow (A.3) [cf. section 2c(2)].

The net $\overline{EKE_{0-1}}$ budgets are characterized in the NAC and SAC regions with spatial averages and spatial distributions of the A.2 and A.3 terms of the $\overline{EKE_{0-1}}$ equation (29) (Fig. 5). They amount to a moderate and an intense net $\overline{EKE_{0-1}}$ source in the NAC (A.2 + A.3: 0.17 10^{-5} m^3 s^{-3}) and the SAC regions (A.2 + A.3: 2.06 10^{-5} m^3 s^{-3}), respectively (Fig. 5, left). This indicates that both regions are locations of mesoscale eddy generation, which are then advected (since the outgoing fluxes are larger than the incoming fluxes: A.2 + A.3 > 0). The net $\overline{EKE_{0-1}}$ budgets have variable patterns within the NAC and SAC regions, resulting from the different contributions of the linear (A.2) and nonlinear (A.3) components of the $\overline{EKE_{0-1}}$ fluxes divergence. This allows us to divide the NAC and SAC into subareas (Fig. 5). These subareas of different mesoscale eddy dynamics also correspond to subareas of different eddy vertical structures (A–D boxes in Fig. 4). We further characterize in the following the processes at the origins of these different eddy vertical structures.

1) THE NORTHERN AGULHAS CURRENT

In the NAC, the net $\overline{EKE_{0-1}}$ budget differs between areas in the path of the Agulhas Current, along the shelf, and offshore in the Subgyre—away from the topographic constraint and from the Agulhas Current (Fig. 5, top left). This makes the NAC a region of moderate mesoscale eddy generation. The net $\overline{EKE_{0-1}}$ sources and sinks are more intense at the shelf, where mesoscale eddies of large $\overline{EKE}$ barotropic component are found, than offshore, where mesoscale eddies having $\overline{EKE}$ barotropic and first baroclinic components in similar proportions are found (Fig. 4, top, and Fig. 5, top left).

The mesoscale eddy energy is mainly transported by the linear $\overline{EKE_{0-1}}$ fluxes (A.2) and follows different evolutions according to the subareas (Fig. 5, top center). The $\overline{EKE_{0-1}}$ transported into the NAC is partially dissipated in the Alongshore Northern Agulhas Current (A.2 < 0, dark purple area), except at the Natal Bight (A.2 > 0, light purple area), and the $\overline{EKE_{0-1}}$ locally gained in the Northern Subgyre is transported outside of the NAC (A.2 > 0, blue area). In the Natal Bight, mesoscale eddies locally gain energy and are then almost equally transported outside of the NAC by the linear and nonlinear $\overline{EKE_{0-1}}$ fluxes (A.2 > 0 and A.3 > 0, light purple area in Fig. 5, top center and top right).
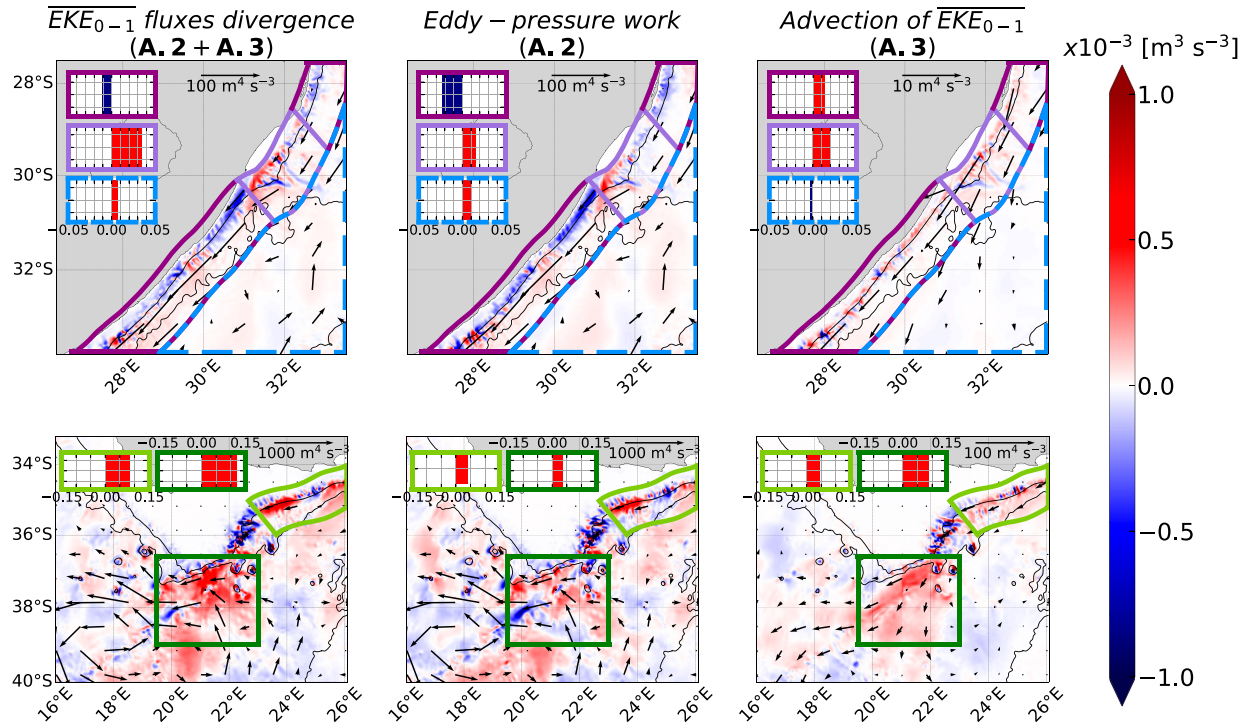
FIG. 5. (left) Net $\overline{EKE_{0-1}}$ budget [A.2 + A.3 in Eq. (29) for $n = 0 + 1$] constituted (center) of the eddy-pressure work (A.2) and (right) of the advection of $\overline{EKE_{0-1}}$ by the total flow (A.3) (m^3 s^{-3}) in the (top) NAC and (bottom) SAC regions. Vector fields denote the $\overline{EKE_{0-1}}$ fluxes (m^4 s^{-3}) (note the scale differences between the advection of $\overline{EKE_{0-1}}$ and the other terms for both regions and between the NAC and SAC regions). The black isolines denote the 1000- and 3000-m isobaths. The NAC and SAC are respectively regions of moderate and intense mesoscale eddy generation, whose energy is then transported away from the regions. The NAC is divided into three subareas: the Alongshore Northern Agulhas Current (dark purple), the Natal Bight (light purple), and the Northern Subgyre (dashed light blue: from the offshore limit of Alongshore Northern Agulhas Current/Natal Bight subareas to the limits of NAC). The SAC is divided into two subareas: the Eastern Agulhas Bank Bight (light green) and off the Agulhas Bank tip (dark green). Spatial averages of the terms over the subareas are shown as barplots. The bars color denotes the sign of the spatially averaged terms (red/blue: positive/negative).

2) THE SOUTHERN AGULHAS CURRENT (SAC)

In the SAC, the positive net $\overline{EKE_{0-1}}$ budgets underline an intense mesoscale eddy generation (Fig. 5, bottom left). The net $\overline{EKE_{0-1}}$ sources are the most intense in the path of the Agulhas Current, where mesoscale eddies of large $\overline{EKE}$ barotropic component are found, compared to the rest of the region, where mesoscale eddies having $\overline{EKE}$ barotropic and first baroclinic components in similar proprotions are found [in the path of the Benguela Current in Fig. 4 (top) and Fig. 5 (bottom)].

Mesoscale eddies locally gain energy in the Eastern Agulhas Bank Bight and off the Agulhas Bank tip (A.2 > 0 and A.3 > 0, light and dark green areas in Fig. 5, bottom center and bottom right). They are then transported by the linear and nonlinear $\overline{EKE_{0-1}}$ fluxes outside of the Eastern Agulhas Bank Bight (A.2 ~ A.3 > 0, light green area) and mainly by the nonlinear $\overline{EKE_{0-1}}$ fluxes outside the Agulhas Bank tip (A.3 > A.2 > 0, dark green area).

The net $\overline{EKE_{0-1}}$ budgets [A.2 and A.2 terms in Eq. (29)] allow to divide the NAC into two subareas of net $\overline{EKE_{0-1}}$ sources and one of net $\overline{EKE_{0-1}}$ sink and the SAC into two subareas of net $\overline{EKE_{0-1}}$ sources. The net $\overline{EKE_{0-1}}$ budgets of these subareas are interpreted in terms of physical processes using the main $\overline{EKE_{0-1}}$ sources and sinks [B, C, and D terms in Eq. (29)] in the following subsection.

b. Main $\overline{EKE_{0-1}}$ sources and sinks (terms B, C, and D)

The right-hand side of the $\overline{EKE_{0-1}}$ equation (29) gathers the $\overline{EKE_{0-1}}$ sources and sinks (B, C, and D terms), which equals the net $\overline{EKE_{0-1}}$ budget (A.2 + A.3 terms) when all summed. The different terms represent the local $\overline{EKE_{0-1}}$ sources and sinks, either coming from the energy transfers between the $\overline{EKE_{0-1}}$, MKE$_{0-1}$ and $\overline{EPE_{0-1}}$ reservoirs (B terms), the energy transfers between the mesoscale ($\overline{EKE_{0-1}}$) and higher baroclinic modes ($\overline{EKE_{2-9}}$, defined as the sum of the $\overline{EKE_n}$ budgets for n ranging from 2 to 9) (C terms), including transfers channeled by topography, or from the local energy generation and dissipation by physical and numerical forcings (D terms). These terms are used as indicator of physical processes [cf. section 2c(2)] and allow us to characterize the eddy dynamics driving the net $\overline{EKE_{0-1}}$ budget.

1) THE NORTHERN AGULHAS CURRENT

The net $\overline{EKE}_{0-1}$ source in the Natal Bight mainly corresponds to the $\overline{HRS}_{0-1}$ contribution (B.1) and more weakly to eddy–mean triad interactions (eddy–mean C.1.1b) (Figs. 6a,b). This $\overline{EKE}_{0-1}$ source is compensated in part by the negative contribution of the advective eddy–mean interactions on slopes (C.3). This term equally transfers energy from $\overline{EKE}$ to MKE within the mesoscale and from $\overline{EKE}$ at mesoscale toward MKE at higher baroclinic modes (light and dark blues, respectively, in Fig. 6a). It therefore supports the mesoscale eddies driving mean currents over sloping bottom (Holloway 1987; Adcock and Marshall 2000) and is mainly interpreted as a transfer between energy reservoirs in this region. Indeed, bottom-intensified flows decompose into a barotropic mode, allowing a nonzero bottom velocity, and into baroclinic modes, to cancel or to shape velocity in the upper layers, as tested by Stanley et al. (2020). In the Natal Bight, mesoscale eddies are generated by the barotropic instability extracting energy from the Agulhas Current (B.1: $MKE_{0-1} \rightarrow \overline{EKE}_{0-1}$) and are strengthened by nonlinear interactions extracting energy from the Agulhas Current across vertical scales (eddy–mean C.1.1b: $MKE_{2-9} \rightarrow \overline{EKE}_{0-1}$). Mesoscale eddies partially transfer back their energy to the mean circulation by an eddy–shelf slope interactions process (C.3: $\overline{EKE}_{0-1} \rightarrow MKE$).

The net $\overline{EKE}_{0-1}$ sink along the 1000-m isobath (Alongshore Northern Agulhas Current in Fig. 5) results from the sum of the negative contributions of $\overline{HRS}_{0-1}$ (B.1), the eddy–mean triad interactions (C.1.1b), the advective eddy–eddy interactions on slopes (C.2), and the vertical mixing (D.1) (Figs. 6a,b). This indicates that mesoscale eddies lose energy to the mean current due to Reynolds stress (B.1) and due to nonlinear eddy–mean interactions transferring energy across vertical scales (eddy–mean C.1.1b). Topography also channels energy loss by transferring energy toward higher baroclinic modes (C.2) and by dissipating eddies barotropic component, which accounts for 60% of the $\overline{EKE}$ at the Northern Agulhas Current branch (Fig. 4), due to bottom friction (D.1). The B.1 and D.1 contributions are typical of currents strongly constrained by topography.

The Natal Bight is the only area in the path of the Agulhas Current being a source of $\overline{EKE}_{0-1}$. In this area, mesoscale eddies are generated by barotropic instability, consistent with the Natal Pulses generation mechanism (Van der Vaart and De Ruijter 2001; Tsugawa and Hasumi 2010; Elipot and Beal 2015) and with mesoscale eddies having a large $\overline{EKE}$ barotropic component ($\phi_0 > \phi_1$ for box A in Fig. 4). In the Alongshore Northern Agulhas Current, the locally generated mesoscale eddies lose energy toward the mean current and eddies of higher baroclinic modes by topographically channeled interactions.

The low net $\overline{EKE}_{0-1}$ source in the Western Subgyre is mainly constituted of the positive contributions of the triad interactions (C.1.1 terms) (Figs. 6a,b). In this offshore area, the effect of the mean current (eddy–mean C.1.1b) weakens and the mesoscale eddies dynamics is dominated by nonlinear interactions between eddy vertical structures (eddy–eddy C.1.1a), which reinforce the mesoscale eddies by realizing an inverse vertical turbulent cascade.

2) THE SOUTHERN AGULHAS CURRENT

The net $\overline{EKE}_{0-1}$ sources in the Eastern Agulhas Bank Bight and off the Agulhas Bank tip include the positive contributions of $\overline{HRS}_{0-1}$ (B.1) and $\overline{VBF}_{0-1}$ (B.3) (Figs. 7a,b). This indicates that mesoscale eddies are generated by mixed baroclinic–barotropic instabilities (B.1 + B.3) triggering downstream of the current separation from the shelf.

In the Eastern Agulhas Bank Bight, the advective eddy–mean interactions on slopes strengthens the mesoscale eddies (C.3 > 0 in Figs. 7a,b). It is interpreted as an energy transfer between vertical modes, because energy is mainly transferred from the MKE at high baroclinic modes to $\overline{EKE}$ at mesoscale. This energy transfer channeled by topography is consistent with mesoscale eddies having a large $\overline{EKE}$ barotropic component (box C in Fig. 4). Here, the mesoscale eddy dynamics is consistent with the shear-edge eddies generation documented by a horizontal shear process controlled by the topography (Lutjeharms et al. 2003a,b).

Off the Agulhas Bank tip, the mesoscale eddies are strengthened by the eddy–mean triad interactions (eddy–mean C.1.1b > 0), consistent with mesoscale eddies having a large $\overline{EKE}$ barotropic component (box D in Fig. 4). The eddy–eddy triad interactions (eddy–eddy C.1.1a < 0) and the advective eddy–mean interactions on slopes (C.3 < 0) partially compensate the mesoscale eddies generation (Figs. 7a,b). The eddy–eddy triad interactions suggest that mesoscale eddies lose a fraction of their energy to eddies of higher baroclinic modes locally where they are generated. The advective eddy–mean interactions on slopes are mainly interpreted as a transfer between energy reservoirs, as in the Natal Bight (in the NAC), because energy is equally transferred from $\overline{EKE}$ to MKE at the mesoscale and from $\overline{EKE}$ at mesoscale to MKE at higher baroclinic modes (light and dark blues, respectively, in Fig. 7a).

The SAC areas, excluding the areas of mesoscale eddy generation (Eastern Agulhas Bank Bight and Agulhas Bank tip), are characterized by a positive contribution of the eddy–eddy triad interactions (eddy–eddy C.1.1a) (Fig. 7b). This indicates that mesoscale eddies are strengthened by nonlinear interactions between vertical structures, realizing an inverse vertical turbulent cascade, while they propagate (vector fields in Fig. 5).

The whole SAC area is characterized by the negative contributions of the vertical mixing (D.1) and of the pressure-gradient eddy–eddy interactions on slopes (C.4) (Fig. 7b).

The vertical mixing (D.1) contribution is not confined to shallow areas (81% of D.1 contribution is in areas of depths > 1000 m) (Fig. 7b). The vertical mixing may therefore be partially attributable to the wind, because the wind dissipates surface energy at all scales (Renault et al. 2018) and the vertical mixing is also a significant sink for smaller vertical structures in this area (Fig. 9, bottom). The vertical mixing is also attributable to the bottom friction, because the barotropic mode accounts for $O(70)\%$ of the $\overline{EKE}$ in the SAC area (Fig. 4).

The pressure gradient eddy–eddy interactions on slopes (C.4) contribution is localized around topography (shelf and seamounts) (Fig. 7b). It represents the $\overline{EKE}$ transfer toward higher baroclinic modes due to the mesoscale eddy scattering

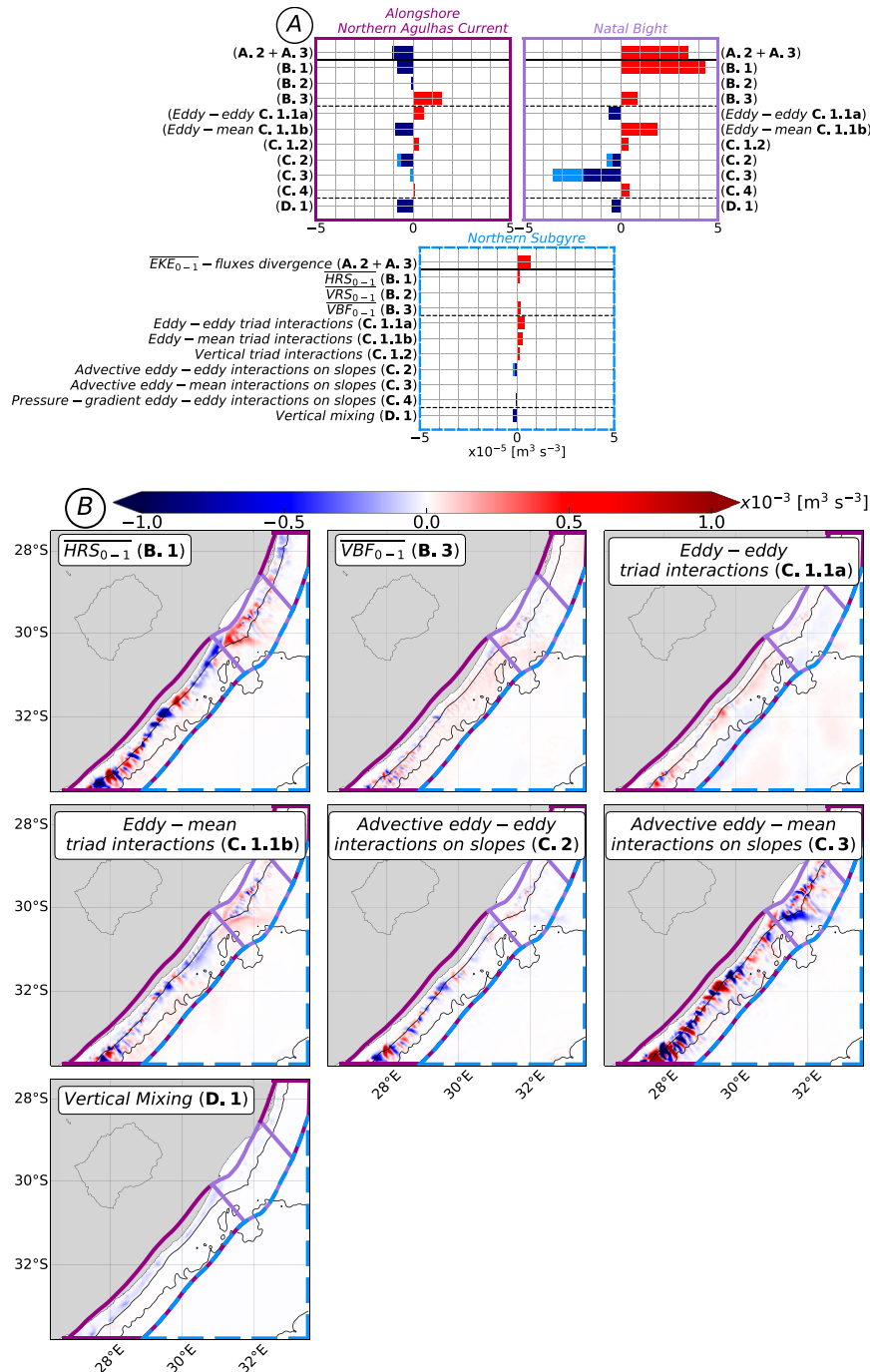FIG. 6. (a) Spatial averages of the contributions of the $\overline{EKE_{0-1}}$ budget [Eq. (29) for $n = 0 + 1$] (m^3 s^{-3}) over the three NAC subareas. It is constituted of the net $\overline{EKE_{0-1}}$ budget (A terms) denoted by a solid black line from the $\overline{EKE_{0-1}}$ sources and sinks (B, C, and D terms) denoted from each other by dotted black lines. The bars color denotes the sign of the spatially averaged terms (red/blue: positive/negative). For the C.2 and C.3 terms, the dark (light) blue color denotes the $n = m \neq l, n = l \neq m, n \neq m = l, n \neq m \neq l$ ($n = m = l$) cases. (b) Maps of the main $\overline{EKE_{0-1}}$ sources and sinks [B, C, and D terms in Eq. (29) for $n = 0 + 1$] (m^3 s^{-3}) in the NAC. The black isolines denote the 1000- and 3000-m isobaths. The Alongshore Agulhas Current (dark purple area) $\overline{EKE_{0-1}}$ sink is constituted of the B.1, eddy–mean C.1.1b, C.2, and D.1 contributions; the Natal Bight (light purple area) $\overline{EKE_{0-1}}$ source is mainly constituted of the B.1 contribution; and the Northern Subgyre (dashed light blue area) $\overline{EKE_{0-1}}$ source is mainly constituted of the eddy–eddy C.1.1a contribution.

over topography, generating internal gravity waves—lee waves (Gill 1982; Nikurashin and Ferrari 2010).

The SAC areas of intense mean current and topography (shelf and seamounts), show intense signals of the eddy–mean triad interactions (eddy–mean C.1.1b) and of the advective eddy–mean interactions on slopes (C.3) (Fig. 7b). The terms compensate between the seamounts faces and there is compensation between the two terms on each face. This double compensation suggests that these signals do not significantly contribute to the net $\overline{EKE}_{0-1}$ budget. The latter compensation likely comes from the separation of the horizontal velocity gradient into a 2D horizontal ($\mathbf{x}$) (C.1.1: eddy–mean triad interactions) and 3D ($\mathbf{x}$, z) (C.3: advective eddy–mean interactions on slopes) components, which are not relevant for areas associated with large-amplitude topography.

The local $\overline{EKE}_{0-1}$ budgets allow to characterize the mesoscale eddy dynamics in different subareas of the NAC and SAC regions. These local dynamics are put into the context of the regional mesoscale eddy dynamics of the Agulhas Current in the following section.

5. Results III: Main processes related to the mesoscale ($n = 0–1$) eddies generation, dissipation, and EKE transfer routes with eddies of higher baroclinic modes ($n = 2–9$) in the Agulhas Current region

We characterize in this section the processes dominating the mesoscale eddies generation, dissipation, and energy transfer routes with eddies of higher baroclinic modes in the Agulhas Current region. We characterize first the local processes dominating the regional mesoscale eddy dynamics using a combined $\overline{EKE}_{0-1}$ budget for the NAC and SAC regions. We then evaluate the potential direct routes of mesoscale eddy energy down to dissipation using $\overline{EKE}_{2-9}$ budgets.

a. Combined $\overline{EKE}_{0-1}$ budget for the NAC and SAC regions (terms B, C, and D)

In the following, a total $\overline{EKE}_{0-1}$ budget is characterized for the Agulhas Current region (NAC and SAC regions combined) with spatial averages of the A terms (net $\overline{EKE}_{0-1}$ budget) and B, C, D terms ($\overline{EKE}_{0-1}$ sources and sinks) of the $\overline{EKE}_{0-1}$ equation [(29) for $n = 0 + 1$] (Fig. 8).

The budget for the NAC and SAC regions combined is dominated by the SAC (not shown) and characterizes the Agulhas Current as a region of intense mesoscale eddy generation (A.2 and A.3 terms in Figs. 5 and 8).

The mean circulation is the main energy source for mesoscale eddies (Fig. 8). They are generated by instability processes, extracting energy from the Agulhas Current (B.1 + B.3: 67% of the total $\overline{EKE}_{0-1}$ source), and they are strengthened by eddy–mean triad interactions across vertical scales (eddy–mean C.1.1b: 33% of the total $\overline{EKE}_{0-1}$ source). The intensity of the mesoscale eddy generation gradually increases downstream: Natal Bight (in NAC), Eastern Agulhas Bank Bight and Agulhas Bank tip (both in SAC) (Figs. 6a and 7a). This agrees with our description of the low and high mesoscale variability of the Northern and Southern Agulhas Current branches, respectively (Fig. 2), and with the characterization of

the transition between the two branches by Tedesco et al. (2019). Mesoscale eddies are strengthened in the Natal Bight (in NAC) and off the Agulhas Bank tip (in SAC) (Figs. 6a,b and 7a,b).

Locally generated mesoscale eddies energy is then significantly transported away from the region of the Agulhas Current (A.2 + A.3: 46% of the total $\overline{EKE}_{0-1}$ source) and significantly decay due to the local contribution of $\overline{EKE}_{0-1}$ sinks (47% of the total $\overline{EKE}_{0-1}$ source). The contributions of the linear and nonlinear components of the $\overline{EKE}_{0-1}$ fluxes divergence to the mesoscale eddy energy transport differ over the Agulhas Current region. In low mesoscale variability areas (Alongshore Northern Agulhas Current and Northern Subgyre, both in NAC) the linear component (A.2) is the main contribution, whereas in high mesoscale variability areas (Natal Bight, in NAC, and Eastern Agulhas Bank Bight and Agulhas Bank tip, both in SAC) the nonlinear component (A.3) has a comparable or a larger contribution than the linear term (Fig. 5).

Locally generated mesoscale eddies energy decays locally mainly due to $\overline{EKE}$ routes channeled by topography (C.2 + C.3 + C.4: 28% of the total $\overline{EKE}_{0-1}$ source) and local dissipation (D.1: 19% of the total $\overline{EKE}_{0-1}$ source). Topography channels energy from mesoscale eddies toward the mean circulation (C.3: 12.5% of the $\overline{EKE}_{0-1}$ source), likely by driving bottom-intensified mean flows over sloping bottom in the Natal Bight (in NAC) and at the Agulhas Bank tip (in SAC). They also channel energy toward eddies of higher baroclinic modes (C.2 and C.4: 3.5% and 12% of the $\overline{EKE}_{0-1}$ source), weakly by nonlinear interactions (C.2) in the NAC and mainly by linear interactions leading to the generation of internal gravity waves (C.4) in the SAC (Figs. 6a,b and 7a,b).

Mesoscale eddies partially dissipate their energy (D.1: 19% of the total $\overline{EKE}_{0-1}$ source) due to bottom friction, affecting their barotropic component and due to the wind, regardless of their vertical structure (Figs. 6a,b and 7a,b).

The total combined $\overline{EKE}_{0-1}$ budget for the NAC and SAC regions provides evidence that topography channels significant $\overline{EKE}_{0-1}$ routes toward eddies of smaller vertical structures, which might subsequently dissipate their energy. These direct energy routes, potentially down to dissipation, are evaluated with $\overline{EKE}_{2-9}$ budgets in the NAC and SAC regions in the following section.

b. EKE transfer routes between mesoscale ($n = 0–1$) and higher baroclinic modes ($n = 2–9$) (terms A, B, C, and D)

In the following, the $\overline{EKE}$ routes between mesoscale eddies ($n = 0–1$) and eddies of higher baroclinic modes ($n = 2–9$: sum over n ranging from 2 to 9) are characterized with spatial averages of the A terms (net $\overline{EKE}_{2-9}$ budget) and B, C, D terms ($\overline{EKE}_{2-9}$ sources and sinks) of the $\overline{EKE}_n$ equation (29) in the NAC and SAC regions (Fig. 9).

1) THE NORTHERN AGULHAS CURRENT (NAC)

In the Alongshore Northern Agulhas Current, the C.2 nonlinear interactions channeled by topography transfer energy from mesoscale eddies toward higher baroclinic modes and can represent a direct route down to dissipation (Fig. 6a).
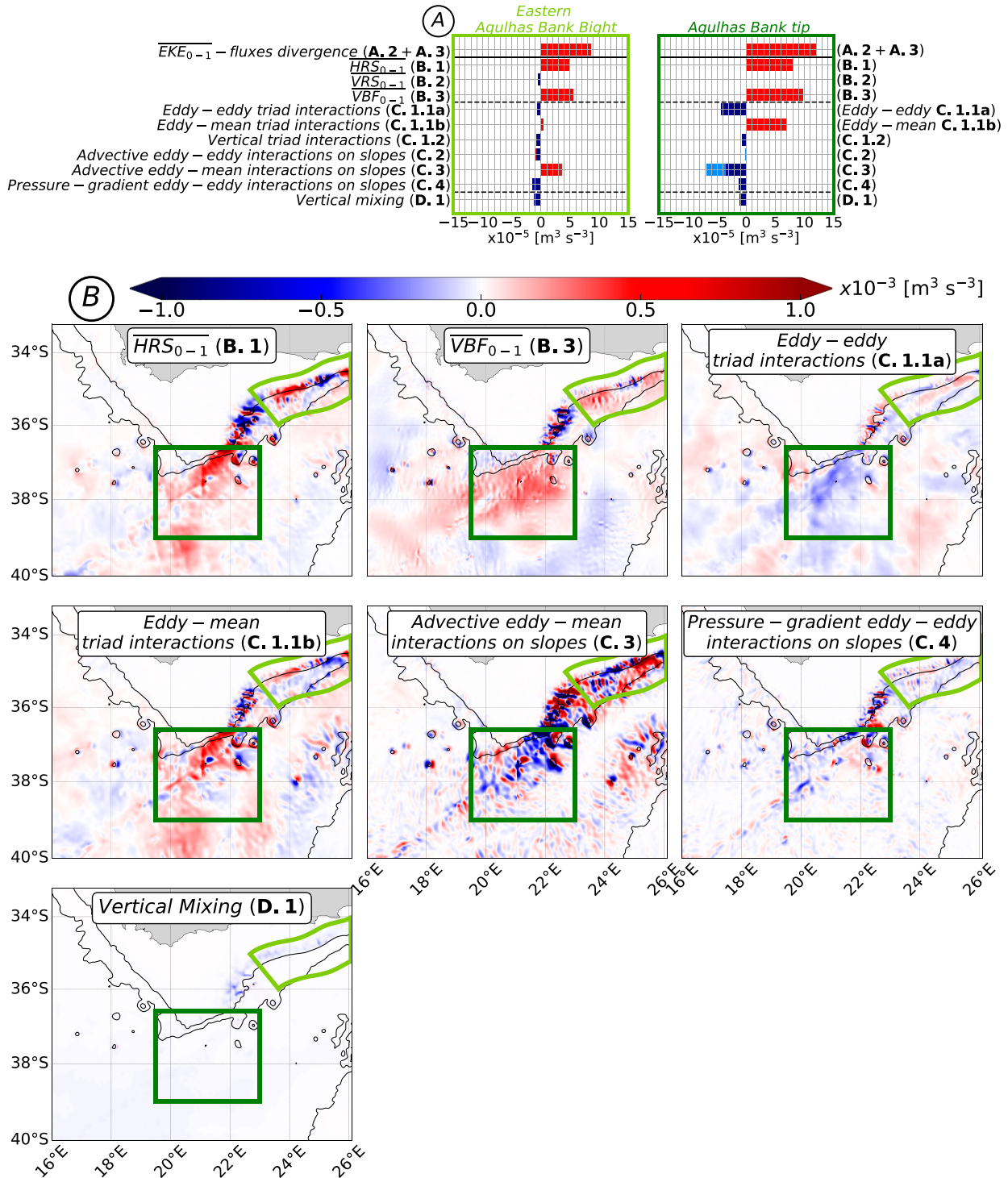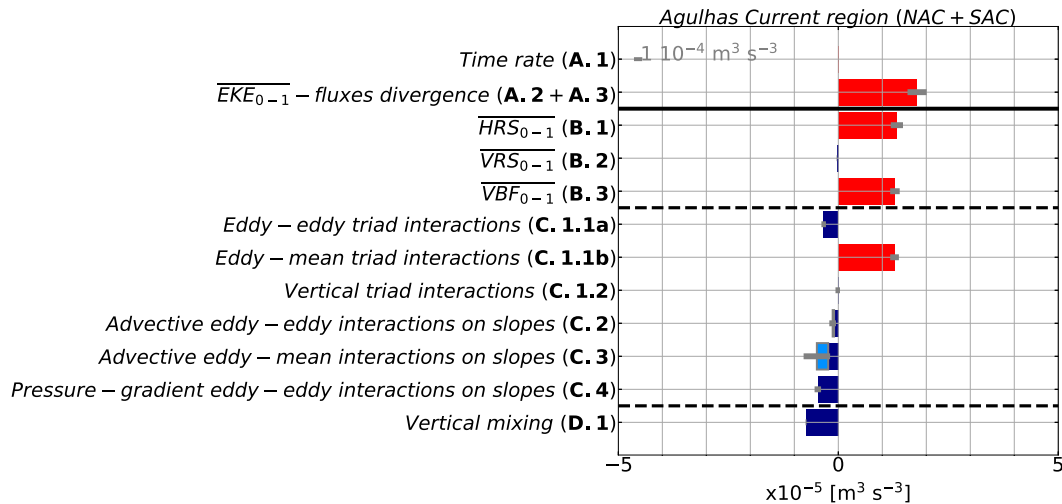
FIG. 7. (a) Spatial averages of the contributions of the $\overline{EKE_{0-1}}$ budget [Eq. (29) for $n = 0 + 1$] (m^3 s^{-3}) over the two SAC subareas. (b) Maps of the main $\overline{EKE_{0-1}}$ sources and sinks [B, C, and D terms in Eq. (29) for $n = 0 + 1$] (m^3 s^{-3}) in the SAC. The black isolines denote the 1000- and 3000-m isobaths. The Eastern Agulhas Bank Bight (light green area) and Agulhas Bank tip (dark green) $\overline{EKE_{0-1}}$ sources are constituted of the B.1, B.3, and C.1.1b contributions, but the C.3 term has an opposite contribution between the two areas. The eddy–eddy C.1.1a has a positive contribution away from the mesoscale eddies generation locations, the C.4 negative contribution is localized around topography and the D.1 negative contribution is spread over the region.

FIG. 8. Spatial averages of the contributions of the $\overline{EKE_{0-1}}$ budget [Eq. (29) for $n = 0 + 1$] ($m^3\ s^{-3}$) over the NAC and SAC regions combined (cf. Fig. 6 for a detailed caption). The gray lines denote the standard deviations of the values (there is a factor 10 between the standard deviations and the spatial averages). The combined $\overline{EKE_{0-1}}$ budget shows that the mean current (B.1 + B.3 and eddy–mean C.1.1b) is the main $\overline{EKE_{0-1}}$ sources. $\overline{EKE_{0-1}}$ locally generated is significantly transported away from the region (A.2 + A.3) and locally decays due to interactions channeled by topography (C.2 + C.3 + C.4) and dissipation (D.1).

The numerical dissipation of high baroclinic modes (D.2$_{2-9}$ in Fig. 9, top left) is locally high in this area, but we cannot conclude on the C.2 contribution realizing a direct energy route down to dissipation. The mean circulation (eddy–mean

C.1.1b$_{2-9}$ + C.3$_{2-9}$ in Fig. 9, top left) represents the main energy source for high baroclinic modes eddies. The numerical dissipation can therefore either affects eddy energy of high baroclinic modes originating from mesoscale eddies or
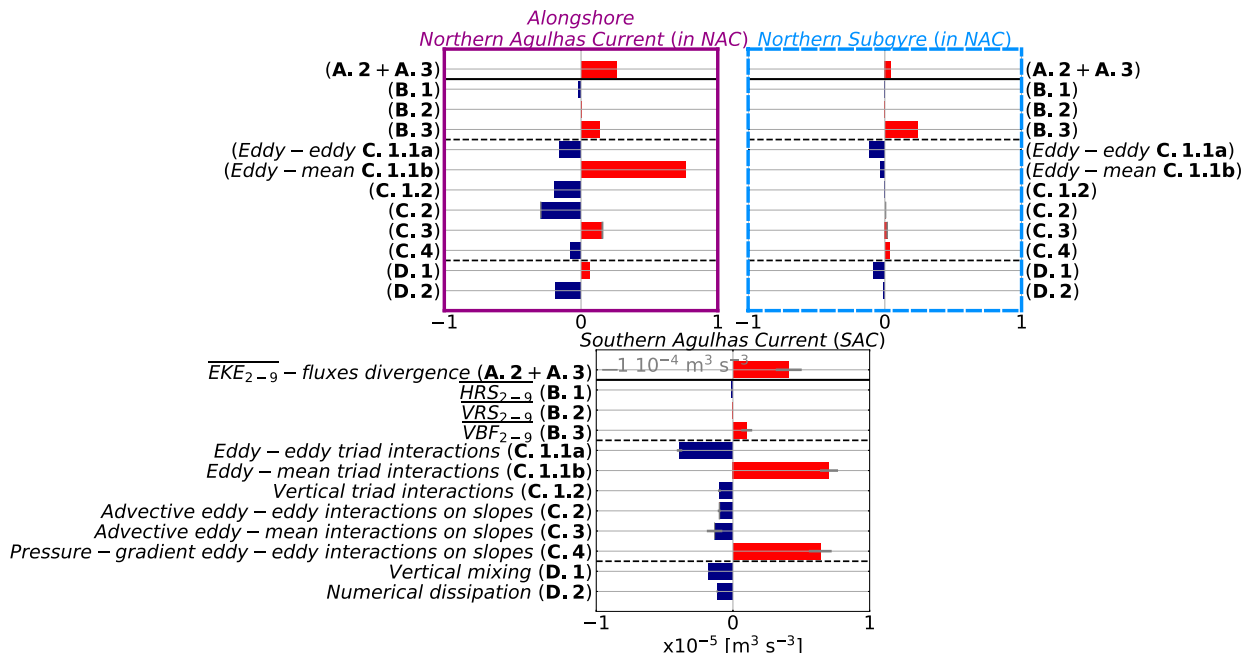
FIG. 9. Spatial averages of the contributions of the $\overline{EKE_{2-9}}$ budget [Eq. (29) for n summed over the range $n = 2$–9] ($m^3\ s^{-3}$) over the Alongshore Northern Agulhas Current and the Northern Subgyre subareas (both in NAC) and the SAC region (cf. Figs. 6 and 8 for a detailed caption). The $\overline{EKE_{0-1}}$ (Fig. 8) and $\overline{EKE_{2-9}}$ budgets are consistent with an inverse vertical cascade fed by submesoscale eddies in the Northern Subgyre (in NAC) and with the internal gravity waves (C.4) as a significant direct route, down to dissipation, by breaking in the SAC. However, they do not allow to conclude on the potential C.2 direct route, down to dissipation, in the Alongshore Northern Agulhas Current (in NAC).

from the mean circulation. The large numerical dissipation of high baroclinic modes is consistent with the eddy vertical structure showing a low variability associated with high baroclinic modes in this region (A box in Fig. 4).

In the Northern Subgyre, an inverse vertical turbulent cascade, likely fed by energy at submesoscale, strengthens mesoscale eddies (Fig. 6a and Fig. 9, top right).

The variability in this region is characterized by mesoscale eddies having $\overline{EKE}$ barotropic and baroclinic components in similar proportions and by surface-intensified eddies with small vertical scales (box B in Fig. 4). The latter ones are generated by baroclinic instability (B.3$_{2-9}$ in Fig. 9, top right) and their energy is partially transferred to mesoscale by eddy–eddy triad interactions (C.1.1a$_{2-9}$ < 0 in Fig. 9, top right, and C.1.1b$_{0-1}$ > 0 in Fig. 6a). This sequence of events is consistent with the submesoscale inverse turbulent cascade described by Schubert et al. (2020) in this region: mixed layer baroclinic instability generates submesoscale eddies, which are subsequently absorbed by mesoscale eddies.

2) THE SOUTHERN AGULHAS CURRENT (SAC)

In the SAC, the C.4 linear interactions channeled by topography transfers energy from mesoscale eddies toward higher baroclinic modes by generating internal gravity waves, which likely represent a significant direct energy route to dissipation (Fig. 7a).

The C.4 process represents a significant energy source for eddies of high baroclinic modes (C.4$_{0-1}$ < 0 and C.4$_{2-9}$ > 0 in Fig. 7a and Fig. 9, bottom). The $\overline{EKE}_{2-9}$ fluxes divergence (A.2$_{2-9}$ + A.3$_{2-9}$ in Fig. 9, bottom) and bottom friction- and wind-induced dissipation as well as numerical dissipation (D.1$_{2-9}$ + D.2$_{2-9}$ in Fig. 9, bottom) show that eddy energy of high baroclinic modes is transported away from the SAC and locally dissipated. It is consistent with the eddy vertical structure showing a low variability associated to high baroclinic modes in this region (C, D, and E boxes in Fig. 4). Both $\overline{EKE}_{0-1}$ and $\overline{EKE}_{2-9}$ budgets are therefore consistent with the internal gravity waves being a significant direct route of mesoscale eddies dissipation by breaking, as characterized for the Southern Ocean (Garabato et al. 2004; Nikurashin and Ferrari 2010; Scott et al. 2011) and for isolated eddies (Evans et al. 2020). Even though we did not quantify the local and nonlocal energy dissipation, due to lee waves and propagating internal breaking waves, respectively, this is likely the main direct route of mesoscale eddy dissipation in the SAC region.

The continuity between the $\overline{EKE}_{0-1}$ and $\overline{EKE}_{2-9}$ budgets is consistent with an inverse vertical cascade in the Northern Subgyre (NAC) and supports the internal gravity waves as the main direct energy route down to dissipation for mesoscale eddies in the SAC.

6. Summary and discussion

a. Summary

In this study, we have characterized the mesoscale eddy energetic dynamics in the region of the Agulhas Current by addressing the following questions: 1) What is the vertical structure of eddy energy? 2) What is the mesoscale EKE budget? 3) What are the processes driving the mesoscale eddies generation, dissipation and EKE transfer routes with eddies of higher baroclinic modes?

The eddy vertical structures are characterized from the eddy energy vertical partitioning ($\overline{EKE_n}$ and $\overline{EAPE_n}$) into the vertical modes categories: $n = 0$, $n = 1$ and $n = 2$–9 (Fig. 4).

In the Agulhas Current and Agulhas Retroflection, the variability is dominated by mesoscale eddies having larger $\overline{EKE}$ barotropic component than the first baroclinic one (large gray disks with solid lines in Fig. 10). Away from intense mean currents (Benguela Current and Subgyre), the variability is characterized by mesoscale eddies having $\overline{EKE}$ barotropic and first baroclinic components in similar proportions (large gray disks with dotted lines in Fig. 10). Similar $\overline{EAPE}$ vertical profiles for regions of intense ($\overline{EAPE_1}$: intensified at intermediate depths) and low ($\overline{EAPE_{2-9}}$: surface intensified) mesoscale variability are found in the Gulf Stream (Vic et al. 2018), suggesting that these $\overline{EAPE}$ vertical structures are generic.

Eddies of higher baroclinic modes represent a significant fraction of the $\overline{EKE}$ (30–35%) in the path of the Agulhas Current, where the current separates from the shelf (~26° and 23°E) and where submesoscale frontal eddies develop (Tedesco et al. 2019) (vortex street of small gray disks at ~26°E in Fig. 10). They represent a significant fraction of the $\overline{EAPE}$ (35%) in the Northern Subgyre—away from the topographic constraint and from the Agulhas Current—where mixed-layer-related turbulence dominates the variability (Schubert et al. 2020) (small gray disk in the Northern Subgyre in Fig. 10).

The mesoscale $\overline{EKE}$ ($\overline{EKE}_{0-1}$) budget is characterized by evaluating separately: the net $\overline{EKE}_{0-1}$ budget [$\overline{EKE}_{0-1}$ fluxes divergence: A.2 and A.3 terms in Eq. (29)] and the $\overline{EKE}_{0-1}$ sources and sinks [B, C, and D categories in Eq. (29)]. The $\overline{EKE}_{0-1}$ budgets for subareas of the NAC and SAC regions (Figs. 5, 6a,b, and 7a,b) and for both regions combined (Fig. 8) were used to characterize the dominating processes driving the mesoscale eddies generation, dissipation and EKE transfer routes with higher baroclinic modes ($n = 2$–9) in the Agulhas Current region.

The Agulhas Current is constituted of a moderate and of an intense region of net $\overline{EKE}_{0-1}$ source (respectively NAC and SAC regions as red boxes in Fig. 10). Mesoscale eddies are locally generated by instability processes of the Agulhas Current, mainly occurring in the SAC (B.1 and B.1 + B.3 as red shaded areas with round and square corners, respectively, in Fig. 10).

Locally generated mesoscale eddies energy is then significantly transported away from the region of the Agulhas Current (A.2 + A.3: 46% of the total $\overline{EKE}_{0-1}$ source in Fig. 8) and it significantly decays locally due to dissipative processes (D.1) and topographically channeled interactions (C.2 + C.3 + C.4) (D.1 + C.2 + C.3 + C.4: 47% of the total $\overline{EKE}_{0-1}$ source in Fig. 8).

Mesoscale eddies energy is locally dissipated due to bottom friction, in the NAC and SAC, and due to the wind, mainly in the SAC (D.1: 19% of the total $\overline{EKE}_{0-1}$ source in Fig. 8).

The $\overline{EKE}$ transfer routes across vertical scales realized by triad and topographically channeled interactions have different contributions to the regional mesoscale eddy dynamics. The eddy–mean triad interactions (eddy–mean C.1.1b as red cross hatching in Fig. 10) significantly strengthen mesoscale eddies along the Agulhas Current, in the NAC and SAC, and
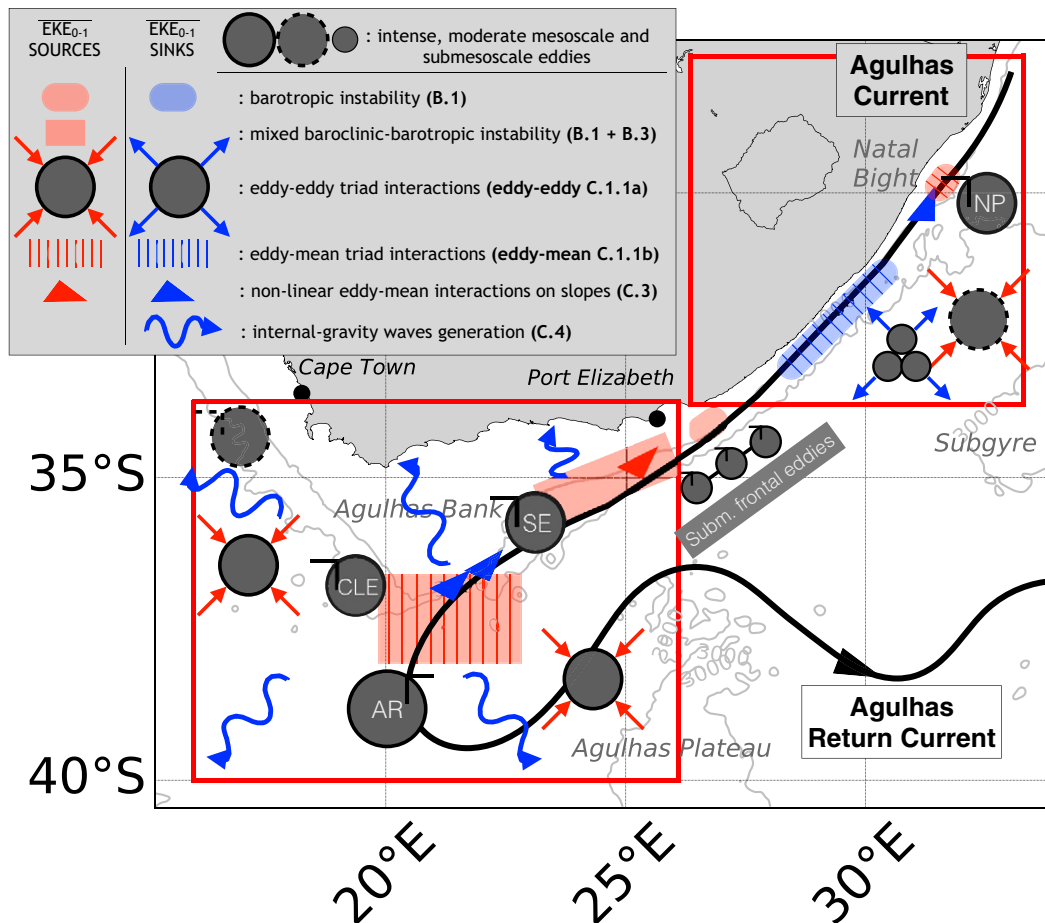
FIG. 10. Scheme of the $\overline{\text{EKE}_{0-1}}$ sources and sinks and related processes in the Agulhas Current region. It focuses on the main processes driving $\overline{\text{EKE}_{0-1}}$ generation and transfers with higher baroclinic modes. The major mean currents (thick black line) and mesoscale eddies of larger $\overline{\text{EKE}}$ barotropic component (large gray disks with solid lines) and of equipartitioned $\overline{\text{EKE}}$ barotropic and first baroclinic components (large gray disks with dotted lines) and submesoscale eddies (small gray disks with solid line) are coarsely located and eddies names are abbreviated this way: Natal Pulse (NP), submesoscale frontal eddies (Subm. frontal eddies), shear-edge eddy (SE), cyclonic lee eddy (CLE), and Agulhas ring (AR). Symbols denote the main processes driving the net $\overline{\text{EKE}_{0-1}}$ sources in the NAC and SAC regions (red boxes). The red (blue) shaded areas denote the mesoscale eddy energy generation (loss) by barotropic instability (B.1 as round corner areas) and by mixed baroclinic–barotropic instability (B.1 + B.3 as squared areas). The red incoming (blue outgoing) arrows from eddies denote eddy–eddy triad interactions realizing a direct (inverse) vertical cascade (eddy–eddy C.1.1a). The red (blue) cross hatching denotes the mesoscale eddy energy gain (loss) by eddy–mean triad interactions transferring energy across vertical scales (eddy–mean C.1.1b). The red (blue) triangular areas denote the mesoscale eddies energy gain (loss) by nonlinear eddy–mean interactions channeled by topography (C.3). The blue oscillating arrows denote the generation of internal gravity waves by mesoscale eddy scattering over topography (C.4). The gray isolines denote the 1000- and 3000-m isobaths. This scheme combines elements of Lutjeharms (2006), Tedesco et al. (2019), and of this study.

the eddy–eddy triad interactions (eddy–eddy C.1.1a as red incoming arrows from the large gray disk in Fig. 10) strengthen mesoscale eddies, by realizing an inverse vertical cascade, away from the topographic constraint and the Agulhas Current, in the NAC and SAC.

The interactions channeled by topography represent a significant EKE sink (C.2 + C.3 + C.4: 28% of the total $\overline{\text{EKE}_{0-1}}$ source in Fig. 8). They channel energy to the mean currents, in the NAC and SAC, by inducing bottom-intensified currents over the sloping bottom (C.3 as blue triangular areas in Fig. 10). They also channel energy to higher baroclinic modes, in the SAC, by generating internal gravity waves (C.4 as blue oscillating arrows in Fig. 10). The C.4 direct $\overline{\text{EKE}_{0-1}}$ route points toward internal gravity waves as the main direct energy route to dissipation for mesoscale eddies in the Agulhas Current region [as for the Southern Ocean; (Garabato et al. 2004; Nikurashin and Ferrari 2010; Scott et al. 2011), and for isolated eddies; (Evans et al. 2020)].

b. Discussion

Our study completes our knowledge of the mesoscale eddy energy balance in the Agulhas Current region and refines the results of recent studies on the mesoscale eddy dynamics in western boundary regions. We can, in particular, test the paradigm of the mesoscale eddies decay upon western boundaries mainly due to direct energy routes, down to dissipation, channeled by topography (Zhai et al. 2010; Chelton et al. 2011; Evans et al. 2020).

Our results characterize the Agulhas Current as a region of mesoscale eddy generation (red boxes in Fig. 10). Mesoscale eddies are generated in the NAC, where the Agulhas Current is strongly constrained by topography (typical of western boundary currents), and in the SAC, where the current separates from the shelf (specific to the Agulhas Current). In the NAC, the mesoscale eddy generation is moderated by a net mesoscale eddy energy sink along the straight and steep shelf slope (blue shaded and cross-hatched area in Fig. 10). This Agulhas Current portion has a mesoscale eddy dynamics seemingly consistent with Zhai et al. (2010).

However, this net energy sink does not dominate the net mesoscale eddy energy budget cumulated in the NAC. Our results show that across the Agulhas Current (NAC and SAC combined), the local mesoscale eddies generation would overcome the local dissipation of mesoscale eddies generated remotely. It suggests a different mesoscale eddy dynamics in the Agulhas Current region than the one suggested by Zhai et al. (2010).

With respect to the local $\overline{EKE_{0-1}}$ sources and sinks [right-hand side of Eq. (29); Figs. 6b, 7b, 8, and 9], the net energy sink in the NAC does not point toward processes realizing direct routes of mesoscale eddy energy down to dissipation, as suggested by Zhai et al. (2010) and shown by Evans et al. (2020). Here, the net mesoscale eddy energy sink is constituted of processes realizing an energy transfer toward the mean currents (B.1 + eddy–mean C.1.1b: 50% of the Alongshore Northern Agulhas Current $\overline{EKE_{0-1}}$ sink in Fig. 6a, as blue shaded and cross-hatched area with round corners in Fig. 10), dissipating energy by bottom friction (D.1: 24% of the Alongshore Northern Agulhas Current $\overline{EKE_{0-1}}$ sink in Fig. 6a) and realizing an energy transfer toward eddies of higher baroclinic modes, without necessarily leading to local energy dissipation (C.2: 18% of the Alongshore Northern Agulhas Current $\overline{EKE_{0-1}}$ sink in Fig. 6a). Our results show that in the presence of a western boundary current, mesoscale eddies lose as much energy to the mean current than to higher baroclinic modes. It refines the understanding of mesoscale eddy decay upon western boundaries.

In the Agulhas Current region, the discrepancies between our study (net mesoscale eddy energy source) and the one of Zhai et al. (2010) (net mesoscale eddy energy sink) come from the different approximations on mesoscale eddies dynamics used to derive the two net $\overline{EKE_{0-1}}$ budgets. We will investigate in a future study the reasons for such differences in this region.

The validity of our results in the context of other western boundary current systems is to consider cautiously, because our study focuses on a western boundary current which has the specificity to separate from the shelf and to retroflect south of 37°E. It would require additional studies of other western boundary currents in order to conclude whether our results, especially the differences with the conclusion of Zhai et al. (2010), are specific to the Agulhas Current or representative of a generic dynamics of western boundary currents.

APPENDIX A

Evaluation of the Modeled Mesoscale Eddy Dynamics Using Surface $\overline{EKE}$ Diagnosed from Smoothed Sea Surface Height

The modeled surface $\overline{EKE}$ is used to evaluate the mesoscale eddy dynamics of the $dx \sim 2.5$-km regional numerical simulation against altimetric data (Fig. 2, top right). To deepen our evaluation, we reproduce as closely as possible the diagnostic made from the AVISO data with the numerical outputs (Fig. A1). The modeled $\overline{EKE}$ is computed from geostrophic surface velocities, derived from smoothed sea surface height fluctuations. The smoothing has a length scale of 100 km to mimic the processing of altimetric data by AVISO and the time fluctuations are defined relative to a 1-yr running mean with a 1-month stepping over the 1994–99 period.

Both smoothed modeled and observed $\overline{EKE}$ show the Northern Agulhas branch low mesoscale variability, by weak eddy energy level $[O(<0.05) \text{ m}^2 \text{ s}^{-2}]$, and the Southern Agulhas branch high mesoscale variability, by a gradually increasing eddy energy level downstream of the branch to a maximum at the Retroflection $[O(0.05–0.3) \text{ m}^2 \text{ s}^{-2}]$ (Fig. A1 and Fig. 2, top left). This agreement between modeled and observed eddy energy levels validates the $dx \sim 2.5$-km regional numerical simulation for studying the mesoscale eddy dynamics. The amplitude differences between the smoothed and not smoothed modeled $\overline{EKE}$s point
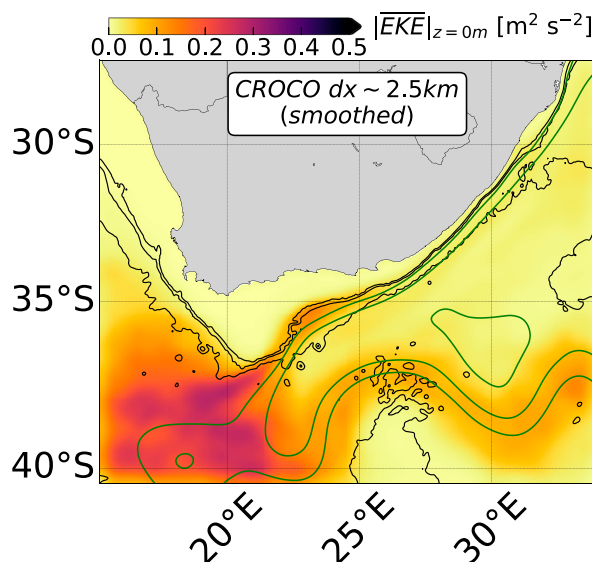
FIG. A1. Surface $\overline{\text{EKE}}$ [m² s⁻²] for CROCO $dx \sim 2.5$ km. $\overline{\text{EKE}}$ is defined from geostrophic velocities diagnosed from the smoothed (length scale of 100 km) sea surface height fluctuations and time fluctuations are defined relatively to a 1-yr running with a 1-month stepping over the 1994–99 period. The green contours denote the 0.25-, 0.5-, 0.75-, and 1-m isolines of mean sea surface height and the black contours denote the 500-, 1000-, and 3000-m isobaths. The patterns and amplitudes of the smoothed modeled $\overline{\text{EKE}}$ denote an Agulhas Current variability in high agreement with the observed one (Fig. 2, top left).

toward areas where smaller scales (<100 km) significantly contribute to the Agulhas Current variability (Fig. A1 and Fig. 2, top right).
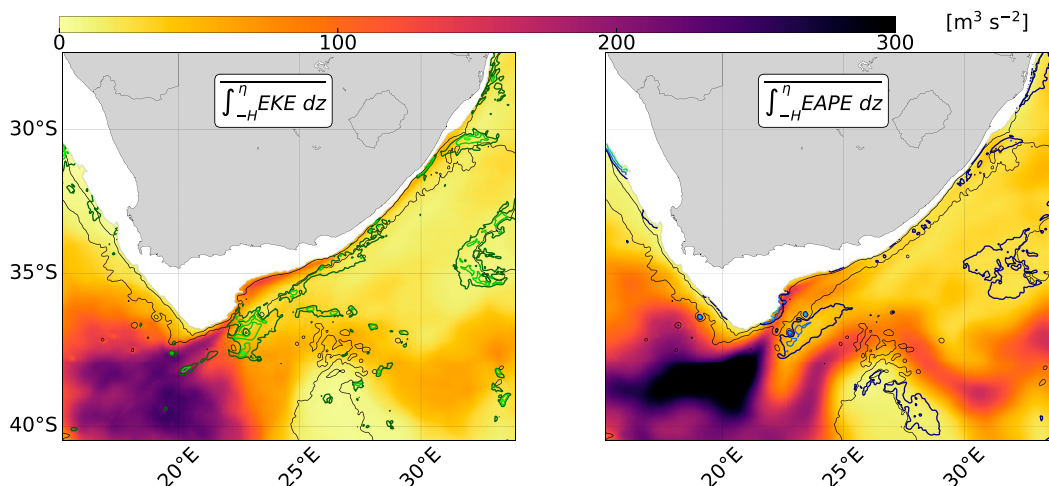
APPENDIX B

Evaluation of the $\overline{\text{EKE}}$ and $\overline{\text{EAPE}}$ Modal Expansions ($\overline{\text{EKE}_n}$ and $\overline{\text{EAPE}_n}$)

The modeled $\overline{\text{EKE}_n}$ [Eq. (16)] and $\overline{\text{EAPE}_n}$ [Eq. (17)] are used to evaluate the validity of the vertical modes decomposition of the $dx \sim 2.5$-km regional numerical simulation, for which the flat-bottom condition is relaxed, and quantify how much of the variability is represented by the first 10 vertical modes. The accuracy of the modeled $\overline{\text{EKE}_n}$ and $\overline{\text{EAPE}_n}$ is measured by the modal expansions residuals (Fig. B1). The residuals are defined as the difference between the total energies $\left(\overline{\int_{-H}^{\eta} \text{EKE}\, dz} \text{ and } \overline{\int_{-H}^{\eta} \text{EAPE}\, dz} \right)$ and their modal expansions $\left(\sum_0^9 \overline{\text{EKE}_n} \text{ and } \sum_0^9 \overline{\text{EAPE}_n} \right)$ normalized by the total energies and converted into percentage.

The agreement between the eddy energy and their modal expansions using the 10 first vertical modes is slightly weaker near bottom for the $\overline{\text{EKE}}$ and near surface for the $\overline{\text{EAPE}}$ (not shown). However, the $\overline{\text{EKE}}$ and $\overline{\text{EAPE}}$ residuals do not exceed 2% and 10% globally over the Agulhas Current region and can reach 5% and 20% in very specific locations. This supports the traditional vertical modes approach as valid in the frame of the $dx \sim 2.5$-km regional simulation and the 10 first vertical modes as accurately representing the modeled dynamics.

APPENDIX C

Evaluation of the Expressions of the Advection and Pressure Gradient Contributions to the $\overline{\text{EKE}_n}$ Budget

The sums of the advection and pressure gradient contributions explicitly computed offline [right-hand sides of (25),
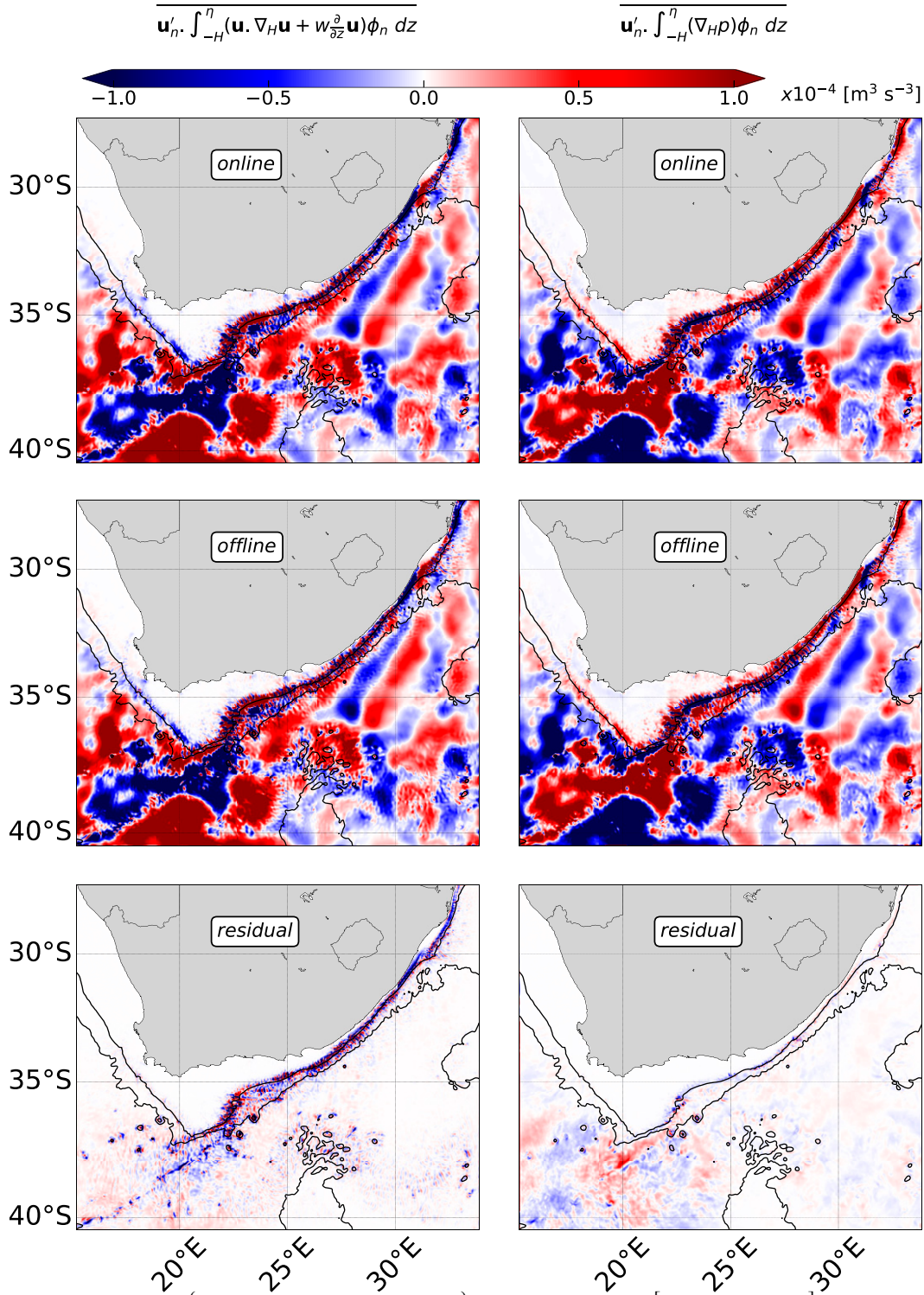

FIG. B1. Vertically integrated (left) $\overline{\text{EKE}}$ and (right) $\overline{\text{EAPE}}$ (m³ s⁻²). The green contours denote the 1% (dark), 2% (light), and 5% (extra light) isolines of $\overline{\text{EKE}}$ residual (left panel), the blue contours denote the 5% (dark), 10% (light), and 20% (extra light) isolines of $\overline{\text{EAPE}}$ residual (right panel), and the black contours denote the 1000- and 3000-m isobaths (all panels). Residuals are a measure of the validity of the modal decomposition of the modeled eddy energies using the 10 first vertical modes. They are defined as the difference between the total energies and their modal expansions normalized by the total energies and converted into percentages (%). With the $\overline{\text{EKE}}$ and $\overline{\text{EAPE}}$ residuals locally peaking at 5% and 20%, respectively, over limited areas, the 10 first vertical modes accurately represent the modeled eddy energies.

FIG. C1. Advection $\left\{\overline{\mathbf{u}'_n \int_{-H}^{\eta} [\mathbf{u} \cdot \nabla_H \mathbf{u} + w(\partial/\partial z)\mathbf{u}]\phi_n \, dz}\right\}$ and pressure gradient $\left[\overline{\mathbf{u}'_n \int_{-H}^{\eta} (\nabla_H p)\phi_n \, dz}\right]$ contributions of the $\overline{\mathrm{EKE}_n}$ budget [Eq. (24)] (m^3 s^{-3}) for the mesoscale ($n = 0 + 1$). Advection and pressure gradient contributions are diagnosed (top) using the online momentum diagnostics [Eq. (24)] and (middle) as the sum of the advection (25) and pressure gradient (27) subcontributions explicitly diagnosed offline. (bottom) The online and offline diagnostics differ by lower-order residuals, which originate from their different time sampling and spatial derivative discretization.
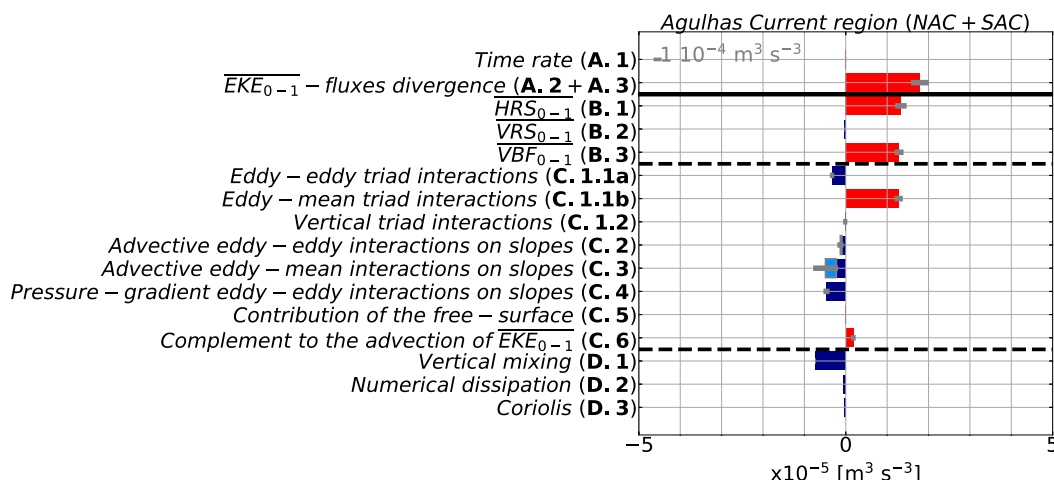
FIG. D1. Spatial averages of all contributions of the $\overline{EKE_{0-1}}$ budget [Eq. (29) for $n = 0 + 1$] (m^3 s^{-1}) over the NAC and SAC regions combined (cf. Figs. 6 and 8 for a detailed caption). The $\overline{EKE_{0-1}}$ budget is derived, from the $dx \sim$ 2.5-km grid numerical outputs, using the residual method to preserve the numerical accuracy of its closure. The physical and numerical contributions of the C.5, C.6, D.2, and D.3 terms as well as the A.1 term represent a low contribution to the net $\overline{EKE_{0-1}}$ budget (A.2 + A.3). They therefore are not included in the discussion of the $\overline{EKE_{0-1}}$ budget.

(26), and (27), respectively] are compared to the term computed from the online advection and pressure gradient diagnostics [left-hand sides of (25), (26), and (27), respectively] to evaluate the accuracy of the analytical developments of the contributions of the horizontal (25) and vertical advection terms (26) and of the pressure gradient term (27) for the mesoscale ($n = 0–1$) (Fig. C1).

The offline and online advection and pressure gradient terms show patterns and magnitudes in good agreement at first order, but the second-order residuals (24% and 6%, respectively) do not allow for the $\overline{EKE_{0-1}}$ budget to close. The time sampling difference between the online and the offline diagnostics contribute to the second-order residual. The subinertial dynamics is filtered from the offline terms which are computed from the numerical outputs (daily averages). The different finite difference schemes used for discretizing the spatial derivatives between the online and the offline diagnostics also contributes to the second-order residual.

APPENDIX D

Mesoscale $\overline{EKE_n}$ ($\overline{EKE_{0-1}}$) Budget in the $dx \sim$ 2.5-km Regional Numerical Simulation: Closure and Main Contributions

The numerical accuracy of the $\overline{EKE_n}$ budget [Eq. (29)] closure is preserved by computing the advection (25), (26) and pressure gradient contributions (27) from the residual method. This method consists in explicitly computing offline all the contributions of the advection and the pressure gradient terms except one, computed as a residual between the sum of the explicitly computed offline contributions and the advection and pressure gradient terms computed using online momentum diagnostics. To limit the offline

computation of spatial derivatives, the horizontal advection of $\overline{EKE_n}$ (component of A.3) and the eddy-pressure work (A.2) are determined as residuals. The $\overline{EKE_n}$ budget closure is evaluated by the ratio between the root-mean-square of the budget residual, defined as the difference between the time rate (A.1) and the sum of the rest of the $\overline{EKE_n}$ terms (from A.2 to D.3), and the root-mean-square of the time rate (A.1). It is of 8×10^{-5} for the mesoscale ($n = 0–1$) and attests of the closure of the $\overline{EKE_{0-1}}$ budget derived from the $dx \sim$ 2.5-km grid numerical outputs.

The different contributions to the $\overline{EKE_n}$ budget in the Agulhas Current region, computed using the residual method, are evaluated by the spatial averages of all the terms of the $\overline{EKE_n}$ budget (A, B, C, and D terms) computed over the NAC and SAC regions combined (Fig. D1).

The combination of the contribution of the free-surface (C.5), the complement to the advection of $\overline{EKE_n}$ (C.6), the numerical dissipation (D.2) and Coriolis (D.3) together represents a low contribution (5%) to the net $\overline{EKE_{0-1}}$ budget (left-hand side of the $\overline{EKE_n}$ equation: A.1 + A.2 + A.3) compared to the other $\overline{EKE_n}$ sources and sinks (right-hand side of the $\overline{EKE_n}$ equation: B, C, and D). It confirms that the terms C.5 and C.6 are not related to explicit physical processes and that the numerical contributions D.2 and D.3 are negligible for the mesoscale eddy dynamics.

In addition, the time rate (A.1) represents a low contribution (0.4%) to the net $\overline{EKE_{0-1}}$ budget compared to the $\overline{EKE_n}$ fluxes divergence (A.2 + A.3). It confirms that the term A.1 tends toward zero for the $dx \sim$ 2.5-km simulation period (1994–99) and therefore that the terms A.2 and A.3 mainly account for the net $\overline{EKE_{0-1}}$ budget.

In the present study, we therefore do not include the A.1, C.5, C.6, D.2, and D.3 terms in the discussion of the $\overline{EKE_{0-1}}$ budgets.

REFERENCES

Adcock, S., and D. Marshall, 2000: Interactions between geostrophic eddies and the mean circulation over large-scale bottom topography. *J. Phys. Oceanogr.*, **30**, 3223–3238, https://doi.org/10.1175/1520-0485(2000)030<3223:IBGEAT>2.0.CO;2.

Aluie, H., M. Hecht, and G. Vallis, 2018: Mapping the energy cascade in the North Atlantic Ocean: The coarse-graining approach. *J. Phys. Oceanogr.*, **48**, 225–244, https://doi.org/10.1175/JPO-D-17-0100.1.

Arbic, B., K. Polzin, R. Scott, J. Richman, and J. Shriver, 2013: On eddy viscosity, energy cascades, and the horizontal resolution of gridded satellite altimeter products. *J. Phys. Oceanogr.*, **43**, 283–300, https://doi.org/10.1175/JPO-D-11-0240.1.

——, M. Müller, J. Richman, J. Shriver, A. Morten, R. Scott, G. Sérazin, and T. Penduff, 2014: Geostrophic turbulence in the frequency–wavenumber domain: Eddy-driven low-frequency variability. *J. Phys. Oceanogr.*, **44**, 2050–2069, https://doi.org/10.1175/JPO-D-13-054.1.

Beal, L., S. Elipot, A. Houk, and G. Leber, 2015: Capturing the transport variability of a western boundary jet: Results from the Agulhas Current Time-Series Experiment (ACT). *J. Phys. Oceanogr.*, **45**, 1302–1324, https://doi.org/10.1175/JPO-D-14-0119.1.

Capet, X., J. McWilliams, M. Molemaker, and A. Shchepetkin, 2008: Mesoscale to submesoscale transition in the California Current System. Part III: Energy balance and flux. *J. Phys. Oceanogr.*, **38**, 2256–2269, https://doi.org/10.1175/2008JPO3810.1.

Charney, J. G., 1971: Geostrophic turbulence. *J. Atmos. Sci.*, **28**, 1087–1095, https://doi.org/10.1175/1520-0469(1971)028<1087:GT>2.0.CO;2.

Chelton, D., R. Deszoeke, M. Schlax, K. E. Naggar, and N. Siwertz, 1998: Geographical variability of the first baroclinic Rossby radius of deformation. *J. Phys. Oceanogr.*, **28**, 433–460, https://doi.org/10.1175/1520-0485(1998)028<0433:GVOTFB>2.0.CO;2.

——, M. Schlax, and R. Samelson, 2011: Global observations of nonlinear mesoscale eddies. *Prog. Oceanogr.*, **91**, 167–216, https://doi.org/10.1016/j.pocean.2011.01.002.

Clément, L., E. Frajka-Williams, K. Sheen, J. Brearley, and A. Garabato Naveira, 2016: Generation of internal waves by eddies impinging on the western boundary of the North Atlantic. *J. Phys. Oceanogr.*, **46**, 1067–1079, https://doi.org/10.1175/JPO-D-14-0241.1.

D'Asaro, E., C. Lee, L. Rainville, R. Harcourt, and L. Thomas, 2011: Enhanced turbulence and energy dissipation at ocean fronts. *Science*, **332**, 318–322, https://doi.org/10.1126/science.1201515.

Debreu, L., P. Marchesiello, P. Penven, and G. Chambon, 2012: Two-way nesting in split-explicit ocean models: Algorithms, implementation and validation. *Ocean Modell.*, **49–50**, 1–21, https://doi.org/10.1016/j.ocemod.2012.03.003.

Dee, D., and Coauthors, 2011: The ERA-Interim reanalysis: Configuration and performance of the data assimilation system. *Quart. J. Roy. Meteor. Soc.*, **137**, 553–597, https://doi.org/10.1002/qj.828.

Dewar, W., and A. Hogg, 2010: Topographic inviscid dissipation of balanced flow. *Ocean Modell.*, **32**, 1–13, https://doi.org/10.1016/j.ocemod.2009.03.007.

——, J. McWilliams, and M. Molemaker, 2015: Centrifugal instability and mixing in the California Undercurrent. *J. Phys.*

Oceanogr., **45**, 1224–1241, https://doi.org/10.1175/JPO-D-13-0269.1.

Duncombe Rae, C. M., 1991: Agulhas retroflection rings in the South Atlantic Ocean: An overview. *S. Afr. J. Mar. Sci.*, **11**, 327–344, https://doi.org/10.2989/025776191784287574.

Eden, C., and H. Dietze, 2009: Effects of mesoscale eddy/wind interactions on biological new production and eddy kinetic energy. *J. Geophys. Res.*, **114**, C05023, https://doi.org/10.1029/2008JC005129.

Elipot, S., and L. M. Beal, 2015: Characteristics, energetics, and origins of Agulhas Current meanders and their limited influence on ring shedding. *J. Phys. Oceanogr.*, **45**, 2294–2314, https://doi.org/10.1175/JPO-D-14-0254.1.

Evans, D., E. Frajka-Williams, A. N. Garabato, K. Polzin, and A. Forryan, 2020: Mesoscale eddy dissipation by a 'zoo' of submesoscale processes at a western boundary. *J. Geophys. Res. Oceans*, **125**, e2020JC016246, https://doi.org/10.1029/2020JC016246.

Fairall, C., E. Bradley, D. Rogers, J. Edson, and G. Young, 1996: Bulk parameterization of air-sea fluxes for tropical ocean-global atmosphere coupled-ocean atmosphere response experiment. *J. Geophys. Res.*, **101**, 3747–3764, https://doi.org/10.1029/95JC03205.

Ferrari, R., and C. Wunsch, 2009: Ocean circulation kinetic energy: Reservoirs, sources, and sinks. *Annu. Rev. Fluid Mech.*, **41**, 253–282, https://doi.org/10.1146/annurev.fluid.40.111406.102139.

——, and ——, 2010: The distribution of eddy kinetic and potential energies in the global ocean. *Tellus*, **62A**, 92–108, https://doi.org/10.3402/tellusa.v62i2.15680.

Fu, L. L., and G. R. Flierl, 1980: Nonlinear energy and enstrophy transfers in a realistically stratified ocean. *Dyn. Atmos. Oceans*, **4**, 219–246, https://doi.org/10.1016/0377-0265(80)90029-9.

Garabato, A. N., K. Polzin, B. King, K. Heywood, and M. Visbeck, 2004: Widespread intense turbulent mixing in the southern ocean. *Science*, **303**, 210–213, https://doi.org/10.1126/science.1090929.

Gill, A., 1982: *Atmosphere–Ocean Dynamics.* Academic Press, 662 pp.

Goschen, W., and E. Schumann, 1990: Agulhas current variability and inshore structures off the Cape Province, South Africa. *J. Geophys. Res.*, **95**, 667–678, https://doi.org/10.1029/JC095iC01p00667.

Gründlingh, M., 1978: Drift of a satellite-tracked buoy in the southern Agulhas Current and Agulhas Return Current. *Deep-Sea Res.*, **25**, 1209–1224, https://doi.org/10.1016/0146-6291(78)90014-0.

Gula, J., and V. Zeitlin, 2010: Instabilities of buoyancy-driven coastal currents and their nonlinear evolution in the two-layer rotating shallow-water model. Part 1. Passive lower layer. *J. Fluid Mech.*, **659**, 69–93, https://doi.org/10.1017/S0022112010002405.

——, M. Molemaker, and J. McWilliams, 2015a: Gulf Stream dynamics along the southeastern U.S. seaboard. *J. Phys. Oceanogr.*, **45**, 690–715, https://doi.org/10.1175/JPO-D-14-0154.1.

——, ——, and ——, 2015b: Topographic vorticity generation, submesoscale instability and vortex street formation in the Gulf Stream. *Geophys. Res. Lett.*, **42**, 4054–4062, https://doi.org/10.1002/2015GL063731.

——, ——, and ——, 2016: Topographic generation of submesoscale centrifugal instability and energy dissipation. *Nat. Commun.*, **7**, 12811, https://doi.org/10.1038/ncomms12811.

Haidvogel, D. B., and A. Beckmann, 1999: *Numerical Ocean Circulation Modeling.* World Scientific, 344 pp.

Harrison, D. E., and A. R. Robinson, 1978: Energy analysis of open regions of turbulent flows–Mean eddy energetics of a numerical ocean circulation experiment. *Dyn. Atmos. Oceans*, **2**, 185–211, https://doi.org/10.1016/0377-0265(78)90009-X.

Holloway, G., 1987: Systematic forcing of large-scale geophysical flows by eddy-topography interaction. *J. Fluid Mech.*, **184**, 463–476, https://doi.org/10.1017/S0022112087002970.

Hughes, C., and C. Wilson, 2008: Wind work on the geostrophic ocean circulation: An observational study of the effect of small scales in the wind stress. *J. Geophys. Res.*, **113**, C02016, https://doi.org/10.1029/2007JC004371.

Kelly, S., 2016: The vertical mode decomposition of surface and internal tides in the presence of a free surface and arbitrary topography. *J. Phys. Oceanogr.*, **46**, 3777–3788, https://doi.org/10.1175/JPO-D-16-0131.1.

——, J. Nash, and E. Kunze, 2010: Internal-tide energy over topography. *J. Geophys. Res.*, **115**, C06014, https://doi.org/10.1029/2009JC005618.

——, ——, K. Martini, H. Alford, and E. Kunze, 2012: The cascade of tidal energy from low to high modes on a continental slope. *J. Phys. Oceanogr.*, **42**, 1217–1232, https://doi.org/10.1175/JPO-D-11-0231.1.

Khatri, H., J. Sukhatme, A. Kumar, and M. Verma, 2018: Surface ocean enstrophy, kinetic energy fluxes, and spectra from satellite altimetry. *J. Geophys. Res. Oceans*, **123**, 3875–3892, https://doi.org/10.1029/2017JC013516.

Krug, M., J. Tournadre, and F. Dufois, 2014: Interactions between the Agulhas Current and the eastern margin of the Agulhas Bank. *Cont. Shelf Res.*, **81**, 67–79, https://doi.org/10.1016/j.csr.2014.02.020.

LaCasce, J., 2017: The prevalence of oceanic surface modes. *Geophys. Res. Lett.*, **44**, 11 097–11 105, https://doi.org/10.1002/2017GL075430.

Lahaye, N., S. Llewellyn, and G. Stefan, 2020: Modal analysis of internal wave propagation and scattering over large-amplitude topography. *J. Phys. Oceanogr.*, **50**, 305–321, https://doi.org/10.1175/JPO-D-19-0005.1.

Lutjeharms, J., 2006: *The Agulhas Current.* Springer, 329 pp.

——, and H. Valentine, 1988: Eddies at the subtropical convergence south of Africa. *J. Phys. Oceanogr.*, **18**, 761–774, https://doi.org/10.1175/1520-0485(1988)018<0761:EATSCS>2.0.CO;2.

——, and I. Ansorge, 2001: The Agulhas return current. *J. Mar. Syst.*, **30**, 115–138, https://doi.org/10.1016/S0924-7963(01)00041-0.

——, R. Catzel, and H. Valentine, 1989: Eddies and other boundary phenomena of the Agulhas Current. *Cont. Shelf Res.*, **9**, 597–616, https://doi.org/10.1016/0278-4343(89)90032-0.

——, O. Boebel, and H. Rossby, 2003a: Agulhas cyclones. *Deep-Sea Res. II*, **50**, 13–34, https://doi.org/10.1016/S0967-0645(02)00378-8.

——, P. Penven, and C. Roy, 2003b: Modelling the shear edge eddies of the southern Agulhas Current. *Cont. Shelf Res.*, **23**, 1099–1115, https://doi.org/10.1016/S0278-4343(03)00106-7.

Masuda, A., 1978: Group velocity and energy transport by Rossby waves. *J. Oceanogr.*, **34**, 1–7, https://doi.org/10.1007/BF02109610.

McWilliams, J. C., 2016: Submesoscale currents in the ocean. *Proc. Roy. Soc.*, **472A**, 20160117, https://doi.org/10.1098/rspa.2016.0117.

Molemaker, M., J. McWilliams, and X. Capet, 2010: Balanced and unbalanced routes to dissipation in an equilibrated Eady

flow. *J. Fluid Mech.*, **654**, 35–63, https://doi.org/10.1017/S0022112009993272.

Müller, P., J. McWilliams, and M. Molemaker, 2005: Routes to dissipation in the ocean: The two-dimensional/three-dimensional turbulence conundrum. *Marine Turbulence: Theories, Observations and Models*, H. Z. Baumert, J. H. Simpson, and J. Sündermann, Eds., Cambridge University Press, 397–405.

Nikurashin, M., and R. Ferrari, 2010: Radiation and dissipation of internal waves generated by geostrophic motions impinging on small-scale topography: Theory. *J. Phys. Oceanogr.*, **40**, 1055–1074, https://doi.org/10.1175/2009JPO4199.1.

——, and ——, 2011: Global energy conversion rate from geostrophic flows into internal lee waves in the deep ocean. *Geophys. Res. Lett.*, **38**, L08610, https://doi.org/10.1029/2011GL046576.

Paldor, N., and J. Lutjeharms, 2009: Why is the stability of the Agulhas Current geographically bi-modal? *Geophys. Res. Lett.*, **36**, L14604, https://doi.org/10.1029/2009GL038445.

Renault, L., J. McWilliams, and P. Penven, 2017: Modulation of the Agulhas Current retroflection and leakage by oceanic current interaction with the atmosphere in coupled simulations. *J. Phys. Oceanogr.*, **47**, 2077–2100, https://doi.org/10.1175/JPO-D-16-0168.1.

——, ——, and J. Gula, 2018: Dampening of submesoscale currents by air-sea stress coupling in the Californian upwelling system. *Sci. Rep.*, **8**, 13388, https://doi.org/10.1038/s41598-018-31602-3.

Rhines, P., 1977: The dynamics of unsteady currents. *Marine Modeling*, E. D. Goldberg et al., Eds., *The Sea—Ideas and Observations on Progress in the Study of the Seas*, Vol. 6, John Wiley and Sons, 189–318.

——, 1979: Geostrophic turbulence. *Annu. Rev. Fluid Mech.*, **11**, 401–441, https://doi.org/10.1146/annurev.fl.11.010179.002153.

Rocha, C., G. Wagner, and W. Young, 2018: Stimulated generation: Extraction of energy from balanced flow by near-inertial waves. *J. Fluid Mech.*, **847**, 417–451, https://doi.org/10.1017/jfm.2018.308.

Rouault, M., and P. Penven, 2011: New perspectives on Natal Pulses from satellite observations. *J. Geophys. Res. Oceans*, **116**, C07013, https://doi.org/10.1029/2010JC006866.

Roullet, G., 2020: World Ocean Atlas of Argo inferred statistics. SEANOE, accessed 9 March 2020, https://doi.org/10.17882/72432.

——, X. Capet, and G. Maze, 2014: Global interior eddy available potential energy diagnosed from Argo floats. *Geophys. Res. Lett.*, **41**, 1651–1656, https://doi.org/10.1002/2013GL059004.

Rubio, A., B. Blanke, S. Speich, N. Grima, and C. Roy, 2009: Mesoscale eddy activity in the southern Benguela upwelling system from satellite altimetry and model data. *Prog. Oceanogr.*, **83**, 288–295, https://doi.org/10.1016/j.pocean.2009.07.029.

Salmon, R., 1980: Baroclinic instability and geostrophic turbulence. *Geophys. Astrophys. Fluid Dyn.*, **15**, 167–211, https://doi.org/10.1080/03091928008241178.

Schlösser, F., and C. Eden, 2007: Diagnosing the energy cascade in a model of the North Atlantic. *Geophys. Res. Lett.*, **34**, L02604, https://doi.org/10.1029/2006GL027813.

Schubert, R., J. Gula, R. Greatbatch, B. Baschek, and A. Biastoch, 2020: The submesoscale kinetic energy cascade: Mesoscale absorption of submesoscale mixed layer eddies and frontal downscale fluxes. *J. Phys. Oceanogr.*, **50**, 2573–2589, https://doi.org/10.1175/JPO-D-19-0311.1.

Scott, R. B., and F. Wang, 2005: Direct evidence of an oceanic inverse kinetic energy cascade from satellite altimetry. *J. Phys. Oceanogr.*, **35**, 1650–1666, https://doi.org/10.1175/JPO2771.1.

——, and B. K. Arbic, 2007: Spectral energy fluxes in geostrophic turbulence: Implications for ocean energetics. *J. Phys. Oceanogr.*, **37**, 673–688, https://doi.org/10.1175/JPO3027.1.

Scott, R., J. Goff, A. N. Garabato, and A. Nurser, 2011: Global rate and spectral characteristics of internal gravity wave generation by geostrophic flow over topography. *J. Geophys. Res.*, **116**, C09029, https://doi.org/10.1029/2011JC007005.

Sen, A., R. Scott, and B. Arbic, 2008: Global energy dissipation rate of deep-ocean low-frequency flows by quadratic bottom boundary layer drag: Computations from current-meter data. *Geophys. Res. Lett.*, **35**, L09606, https://doi.org/10.1029/2008GL033407.

Seo, H., A. Miller, and J. Norris, 2016: Eddy–wind interaction in the California Current System: Dynamics and impacts. *J. Phys. Oceanogr.*, **46**, 439–459, https://doi.org/10.1175/JPO-D-15-0086.1.

Shchepetkin, A., and J. McWilliams, 2005: The Regional Oceanic Modeling System (ROMS): A split-explicit, free-surface, topography-following- coordinate ocean model. *Ocean Modell.*, **9**, 347–404, https://doi.org/10.1016/j.ocemod.2004.08.002.

Smith, K., and G. Vallis, 2001: The scales and equilibration of midocean eddies: Freely evolving flow. *J. Phys. Oceanogr.*, **31**, 554–571, https://doi.org/10.1175/1520-0485(2001)031<0554:TSAEOM>2.0.CO;2.

Stanley, Z., S. Bachman, and I. Grooms, 2020: Vertical structure of ocean mesoscale eddies with implications for parameterizations of tracer transport. *J. Adv. Model. Earth Syst.*, **12**, e2020MS002151, https://doi.org/10.1029/2020MS002151.

Tedesco, P., J. Gula, C. Ménesguen, P. Penven, and M. Krug, 2019: Generation of submesoscale frontal eddies in the Agulhas Current. *J. Geophys. Res. Oceans*, **124**, 7606–7625, https://doi.org/10.1029/2019JC015229.

Thomas, L., J. Taylor, R. Ferrari, and T. Joyce, 2013: Symmetric instability in the Gulf Stream. *Deep-Sea Res. II*, **91**, 96–110, https://doi.org/10.1016/j.dsr2.2013.02.025.

Tsugawa, M., and H. Hasumi, 2010: Generation and growth mechanism of the Natal Pulse. *J. Phys. Oceanogr.*, **40**, 1597–1612, https://doi.org/10.1175/2010JPO4347.1.

Tulloch, R., J. Marshall, C. Hill, and K. Smith, 2011: Scales, growth rates, and spectral fluxes of baroclinic instability in the ocean. *J. Phys. Oceanogr.*, **41**, 1057–1076, https://doi.org/10.1175/2011JPO4404.1.

Vallis, G., 2006: *Atmospheric and Oceanic Fluid Dynamics: Fundamentals and Large-Scale Circulation.* Cambridge University Press, 745 pp.

Van Aken, H., A. Van Veldhoven, C. Veth, W. De Ruijter, P. Van Leeuwen, S. Drijfhout, C. Whittle, and M. Rouault, 2003: Observations of a young Agulhas ring, Astrid, during MARE in March 2000. *Deep-Sea Res. II*, **50**, 167–195, https://doi.org/10.1016/S0967-0645(02)00383-1.

Van der Vaart, P., and W. De Ruijter, 2001: Stability of western boundary currents with an application to pulselike behavior of the Agulhas Current. *J. Phys. Oceanogr.*, **31**, 2625–2644, https://doi.org/10.1175/1520-0485(2001)031<2625:SOWBCW>2.0.CO;2.

Vic, C., J. Gula, G. Roullet, and F. Pradillon, 2018: Dispersion of deep-sea hydrothermal vent effluents and larvae by submesoscale and tidal currents. *Deep-Sea Res. I*, **133**, 1–18, https://doi.org/10.1016/j.dsr.2018.01.001.

Wunsch, C., 1997: The vertical partition of oceanic horizontal kinetic energy. *J. Phys. Oceanogr.*, **27**, 1770–1794, https://doi.org/10.1175/1520-0485(1997)027<1770:TVPOOH>2.0.CO;2.

Zhai, X., H. Johnson, and D. Marshall, 2010: Significant sink of ocean-eddy energy near western boundaries. *Nat. Geosci.*, **3**, 608–612, https://doi.org/10.1038/ngeo943.